Trophoblast glycoprotein is required for efficient synaptic vesicle exocytosis from retinal rod bipolar cells.

Colin M Wakeham[1], Qing Shi[1], Gaoying Ren[1], Tammie L Haley[1], Robert M Duvoisin[1], Henrique von Gersdorff[2], Catherine W Morgans[1]

[1]Department of Chemical Physiology & Biochemistry, Oregon Health & Science University, Portland, OR 97239, USA

[2]Vollum Institute, Oregon Health & Science University, Portland, OR 97239, USA

Corresponding Author

Catherine W Morgans
Chemical Physiology & Biochemistry, L-334
Oregon Health & Science University
3181 SW Sam Jackson Park Rd
Portland, OR 97239
Email: morgansc@ohsu.edu

Acknowledgements

This work was supported by NIH grants to CWM (R01 EY029985 and P30 EY010572) and HvG (R01 EY014043 and DC012938). The authors would like to thank R Lane Brown, Marc A Meadows, and André A Dagostin for assistance with patch clamp electrophysiology and data analysis. We would also like to thank the OHSU Neuroscience Imaging Center's Ultrastructure and Single Particle Microscopy Core (P30 NS061800) for FIB-SEM data collection.

Author contributions

Study design: CMW, RD, HvG, CWM; Experimentation: CMW, HS, GR, TLH; Data analysis: CMW, HS, RD, HvG, CWM; Figure and manuscript preparation: CMW, HS, RD, HvG, CWM; Editing and review: CMW, RD, HvG, CWM

Conflict of interest statement

The authors declare no competing financial conflicts of interest.

Abstract

Rod bipolar cells (RBCs) faithfully transmit light-driven signals from rod photoreceptors in the outer retina to third order neurons in the inner retina. Recently, significant work has focused on the role of leucine-rich repeat (LRR) proteins in synaptic development and signal transduction at RBC synapses. We previously identified trophoblast glycoprotein (TPBG) as a novel transmembrane LRR protein localized to the dendrites and axon terminals of RBCs. We now examine the effects on RBC physiology and retinal processing of TPBG genetic knockout in mice using immunofluorescence and electrophysiological techniques. The scotopic electroretinogram showed a modest increase in the b-wave and a marked attenuation in oscillatory potentials in the TPBG knockout. No effect of TPBG knockout was observed on the RBC dendritic morphology, TRPM1 currents, or RBC excitability. Because scotopic oscillatory potentials primarily reflect RBC-driven rhythmic activity of the inner retina, we investigated the contribution of TPBG to downstream transmission from RBCs to third-order neurons. Using electron microscopy, we found shorter synaptic ribbons in TPBG knockout axon terminals in RBCs. Time-resolved capacitance measurements indicated that TPBG knockout reduces synaptic vesicle exocytosis and subsequent GABAergic reciprocal feedback without altering voltage-gated Ca^{2+} currents. Thus, TPBG is required for normal synaptic ribbon development and efficient neurotransmitter release from RBCs to downstream cells. Our results highlight a novel synaptic role for TPBG at RBC ribbon synapses and support further examination into the mechanisms by which TPBG regulates RBC physiology.

Graphical abstract

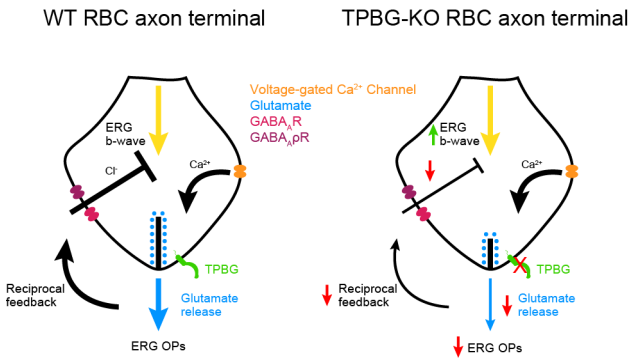

Introduction

Rod bipolar cells (RBCs) receive light-dependent synaptic input from rod photoreceptors in the outer plexiform layer (OPL) and drive retinal output by synapsing with AII amacrine cells (AII-ACs) in the inner plexiform layer (IPL). As the only dedicated bipolar cell in the primary rod visual pathway, RBCs must be able to reliably transmit visual signals over the whole range of rod

64 sensitivity. Accurate transmission of light signals requires precise synaptic targeting and tight
65 control of signal transduction between RBCs and its synaptic partners. Identifying and
66 characterizing the proteins required for the optimization and regulation of RBC synaptic
67 development and function is essential for expanding our understanding of how RBCs contribute
68 to vision.

69 Leucine-rich repeat (LRR) proteins form a large class of transmembrane proteins, each
70 containing multiple leucine-rich motifs arranged to form extracellular protein binding domains
71 (Kobe & Deisenhofer, 1994; Kobe & Kajava, 2001). Several LRR proteins identified in RBCs have
72 been implicated in the development and maintenance of synaptic morphology and function. At
73 synapses between photoreceptors and ON-bipolar cells, LRIT3 and nyctalopin are required for
74 the localization of signal transduction components to the post-synaptic compartment (Cao,
75 Posokhova, & Martemyanov, 2011; Hasan et al., 2019, 2020; Neuillé et al., 2017, 2015; Pearring
76 et al., 2011). In RBC dendrites, LRRTM4 forms a trans-synaptic complex with rod spherules
77 (Agosto & Wensel, 2020), whereas in RBC axon terminals, LRRMT4 is required for functional
78 GABA receptor clustering, reciprocal feedback inhibition, and dyad synapse formation (Sinha et
79 al., 2020). The ELFN family of LRR proteins form trans-synaptic complexes between
80 photoreceptors and bipolar cells without which functioning connections fail to develop and retinal
81 circuitry is mis-wired (Cao et al., 2015, 2020).

82 We recently identified trophoblast glycoprotein (TPBG, also called 5T4 or WAIF1 (Wnt-
83 activated inhibitory factor 1)) in a phosphoproteomics screen as a novel LRR transmembrane
84 glycoprotein in mouse RBCs that undergoes PKCα-dependent phosphorylation (Wakeham et al.,
85 2019). TPBG contains eight N-terminal extracellular LRR motifs and a short intracellular C-
86 terminal tail with a PDZ-interacting domain (Zhao, Malinauskas, Harlos, & Jones, 2014). TPBG
87 localizes to the dendrites and synaptic terminals of RBCs and its expression is closely linked to
88 eye opening and TRPM1 expression, suggesting that TPBG may play a role in RBC development
89 or physiology (Wakeham, Ren, & Morgans, 2020).

90 Because the role of TPBG in the retina has not been established, we sought to
91 characterize the effects of genetic knockout of TPBG in mouse RBCs using immunofluorescence
92 confocal microscopy, electron microscopy, and electrophysiological techniques. RBC synapses
93 form specialized active zones, each containing a synaptic ribbon, that permit a greater bandwidth
94 of information transfer than conventional synapses. Ribbon synapses are noted for tight vesicle-
95 Ca^{2+} coupling and a large supply of readily-available synaptic vesicles tethered close to the active
96 zone (Dieck & Brandstätter, 2006; Morgans, 2000; Moser, Grabner, & Schmitz, 2020). In this
97 study, we report that TPBG is required for normal synaptic ribbon morphology and efficient

synaptic vesicle exocytosis at RBC synapses, implicating TPBG in ribbon synapse development and function.

Methods

Animals and statistical analysis

Constitutive TPBG knockout (TPBG-KO; KO) mice were B6;129S5-Tpbg^{tm1Lex}/Mmucd (MMRRC; UC Davis; Davis, CA, USA; Cat# 031630-UCD; RRID: MMRRC_031630-UCD). KO mice were purchased as cryopreserved sperm and reconstituted into a C57BL/6J (The Jackson Laboratory; Bar Harbor, M; Cat# 000664; RRID: IMSR_JAX:000664) background. Age-matched homozygous wild type (WT) littermates were used as controls. We used mice of both sexes and all mice were maintained on a 12-hour light/dark cycle and provided food and water ad libitum. Animals for immunofluorescence and electroretinogram experiments were 3-6 months old while animals used for patch clamp electrophysiology experiments were three months old. At least three mice were used from each condition for each experiment except for electron microscopy, which used one block per genotype. All animal procedures were in accordance with the National Institutes of Health guidelines and approved by the Oregon Health & Science University Institutional Animal Care and Use Committee.

Statistical analyses were performed in Prism 9 (GraphPad; San Diego, CA, USA) and reported as mean ± SEM. We detected significance between conditions using unpaired Welch's *t*-tests and Brown-Forsythe ANOVA tests. Statistical significance is noted by asterisks (not significant (ns): $p > 0.05$; *: $p < 0.05$; **: $p < 0.01$; ***: $p < 0.001$; ****: $p < 0.0001$).

Immunofluorescence

Fresh eyecups were prepared from dissected eyes by cutting behind the ora serrata and removing the cornea and lens. For sectioning, eyecups were fixed for 30 min by immersion in fresh 4% paraformaldehyde (PFA) in PBS. The fixed eyecups were washed in PBS and then cryoprotected via sequential immersion in 10, 20, and 30% sucrose in PBS. Sections were cut at 20 μm thickness. Retina sections were post-fixed for 10 minutes in 4% PFA, blocked and permeabilized by incubation at room temperature for one hour in antibody incubation solution (AIS; 3% normal horse serum, 0.5% Triton X-100, 0.025% NaN_3 in PBS), and then incubated in primary antibodies diluted in AIS for one hour at room temperature. After washing with PBS, the sections were incubated in secondary antibodies diluted in AIS for one hour at room temperature. The slides were washed again in PBS and then mounted with VECTASHIELD PLUS antifade mounting media with DAPI (Vector Laboratories; Cat# H-2000-10).

132 For whole mount immunofluorescence, eyecups were fixed for 45 min by immersion in
133 fresh 4% PFA in PBS. The fixed eyecups were washed in PBS then retinas were removed prior
134 to blocking and permeabilization for one hour in AIS. The retinas were incubated in primary
135 antibodies diluted in AIS for four days at 4° C then washed overnight in PBST (PBS + 0.05%
136 Triton X-100) at 4° C. Retinas were incubated in secondary antibodies diluted in AIS overnight at
137 4° C then washed again in PBST. Finally, the retinas were mounted with VECTASHIELD PLUS
138 antifade mounting media.
139 Immunofluorescence images were taken with a Leica TCS SP8 X confocal microscope
140 (Leica Biosystems; Wetzlar, Germany) using a Leica HC PL APO CS2 63x/1.40 oil immersion
141 objective (Leica; Cat# 15506350). Brightness and contrast were adjusted equally across
142 genotypes using Fiji (Schindelin et al., 2012). A Gaussian blur using a radius of 0.5 pixels was
143 used to remove graininess from images. See figure legends for specific information on Z-step
144 distance and number of steps. To compare the spatial relationship between presynaptic and
145 postsynaptic proteins in the OPL, ROI lines were drawn across $Ca_v1.4$-GPR179 pairs and the
146 intensity of both fluorescent channels was plotted against the line length in Fiji. The distance
147 between the two fluorescence peaks approximates the distance across the synapse. To examine
148 fluorescent puncta in RBC axon terminals in the IPL, PKCα binaries were created in Fiji using
149 default auto-thresholds to isolate RBC axon terminals. These binaries were then merged with the
150 other channels to remove PKCα-negative puncta. Fluorescent puncta were counted in PKCα-
151 positive axon terminals and normalized to axon terminal area. Mander's colocalization coefficients
152 were calculated using the JACoP plugin in Fiji to compare colocalization patterns between $Ca_v1.4$
153 and RIBEYE puncta after thresholding with Otsu's method. The M1 coefficient was used for the
154 fraction of $Ca_v1.4$ containing RIBEYE and the M2 coefficient was for the fraction of RIBEYE
155 containing $Ca_v1.4$. Colocalization of puncta in PKCα-negative areas was also calculated as a
156 control.
157
158 *Immunoblotting*
159 Retinas were extracted from freshly dissected eyes, suspended in chilled lysis buffer (50
160 mM Tris pH 7.4, 150 mM NaCl, 1 mM EDTA, 1% Triton X-100, 1% deoxycholate, 0.1% SDS) with
161 1X protease/phosphatase inhibitor cocktail (Cell Signaling Technology; Danvers, MA, USA; Cat#
162 5872) and homogenized with a Teflon-glass homogenizer. The lysate was centrifuged for 15
163 minutes at 16,400 rpm and 4° C, and the pellet was discarded. Retinal lysates were diluted to a
164 protein concentration of 1 μg/μl in lysis buffer and brought to 1X NuPAGE LDS Sample Buffer

165 (Thermo Fisher Scientific; Cat# NP0007) and 1X NuPAGE Sample Reducing Agent (Thermo
166 Fisher Scientific; Cat# NP0009). Pre-cast NuPAGE 1 mm 4-12% Bis-Tris gels (Thermo Fisher
167 Scientific; Cat# NP0322BOX) were loaded and run at 200 V and 140 mA for 55 minutes in 1X
168 NuPAGE BOLT SDS Running Buffer (Thermo Fisher Scientific; Cat# B0001).
169 Proteins were transferred onto PVDF membranes using a wet transfer system and 1X
170 NuPAGE Transfer Buffer (Thermo Fisher Scientific; Cat# NP00061) with 5% MeOH at 300 mA
171 for two hours. The membranes were then rinsed with methanol and blocked for one hour in
172 Odyssey Blocking Buffer TBS (LI-COR Biosciences; Cat# 927-50003) on a shaker at room
173 temperature, before being incubated in primary antibody diluted in Odyssey buffer at 4° C
174 overnight. The membranes were washed in TBST (Tris-buffered saline with 0.1% Tween-20),
175 then incubated in secondary antibody diluted in Odyssey buffer for one hour at room temperature
176 before being washed in TBST. Dried blots were imaged using a LI-COR Odyssey CLx Imaging
177 System at 680 and 800 nm.
178
179 *Electron microscopy*
180 Mice were euthanized and enucleated and the retinas were quicky dissected and fixed for
181 30 min by immersion in 3% PFA and 1% glutaraldehyde. The tissue was then processed for
182 electron microscopy using the Dresden protocol (Paridaen, Wilsch-Bräuninger, & Huttner, 2013).
183 Three-dimensional data was acquired using the Helios G3 NanoLab DualBeam FIB-SEM as
184 previous described. Briefly, the resin blocks were trimmed to contain the ganglion cell layer and
185 the IPL near the top edge of the block, mounted to a 45° pre-tilted stub, and coated with 8 nm of
186 carbon. A focused beam of gallium atoms ablated 4 nm off the surface of the sample (FIB
187 conditions: 30 keV accelerating voltage, 790 pA beam current) over the SEM imaging area of 25
188 μm x 10 μm. The freshly ablated surface was then imaged by backscattered electrons using the
189 In-Column Detector (SEM conditions: 3 keV accelerating voltage, 400 pA beam current, 4 nm per
190 pixel, 3 μs dwell time; image resolution: 6144 x 4086, 4 nm isotropic). Ablation and imaging cycles
191 were run over a three-day period resulting in a sample depth of roughly 5 μm (1373 images for
192 the WT dataset and 1284 images for the TPBG-KO dataset). Image stacks were registered using
193 Linear Stack Alignment with the SIFT algorithm in Fiji and cropped to remove alignment artifacts.
194 RBC synaptic terminals were identified by their morphology (size, shape, presence of synaptic
195 ribbons, and arrangement of postsynaptic elements) and their proximity to the ganglion cell layer.
196
197
198

199 *Electroretinogram recording*

200 Mice were dark-adapted overnight and prepared for recording under dim red light.
201 Anesthesia was initiated via IP injection of ketamine:xylazine (100:10 mg/kg) and maintained with
202 booster injections (30:3 mg/kg) at approximately 30 minute intervals until completion of the
203 experiment. Body temperature was maintained at 36.5-38° C. Before recording, the pupils were
204 dilated with 2.5% phenylephrine and 1% tropicamide, and the cornea was anesthetized with 1%
205 topical proparacaine. A wire loop placed under the upper teeth was used to draw the mouse into
206 a custom-made holder that stabilized the head and permitted delivery of 95% O_2/5% CO_2
207 (carbogen; ~0.25 l/min). The recording was made using a custom contact lens electrode featuring
208 a central platinum wire placed against the cornea with a small drop of hypromellose to prevent
209 drying. A loop electrode placed behind the eye served as a reference electrode and a needle
210 electrode placed in the tail served as a ground. The mice were placed in a Ganzfield sphere and
211 light stimuli were provided by custom 502 nm LED photostimulators. Light stimulus intensity was
212 controlled with neutral density filters and by altering flash duration and was measured post-hoc
213 with an ILT5000 radiometer (International Light; Newburyport, MA; USA) using a scotopic filter.
214 Traces were recorded with customized software (ERGLab; Richard Weleber; Casey Eye Institute;
215 Portland, OR, USA).

216 Full-field scotopic electroretinograms (ERGs) from both eyes were recorded
217 simultaneously after a series light flashes ranging from 8.71×10^{-1} to 8.51×10^{1} cd•s/m^2 (-0.06 to
218 1.93 log(cd•s/m^2) (Xiong et al., 2015). For dimmer intensities (-1 to 0 log(cd•s/m^2)), three trials
219 were averaged with inter-flash intervals of 20 seconds. For brighter intensities (0 to 2
220 log(cd•s/m^2)), two trials were averaged with inter-flash intervals of 30 to 120 seconds.

221 ERGLab data was exported for offline processing using a custom Python script and the
222 SciPy package (https://docs.scipy.org/doc). Statistical analyses were performed in Prism 9
223 (GraphPad; San Diego, CA, USA). The start of the flash stimulus was set to time zero and traces
224 were baselined. A-waves and b-waves were isolated using a low-pass filter (60 Hz) and OPs were
225 isolated with a Butterworth band-pass filter (30-300 Hz) and the "signal.filtfilt" function in SciPy
226 (**Figure 2: Supplementary Figure 1**). The a-wave amplitudes were measured from baseline-to-
227 trough, b-wave amplitudes were measured from a-wave trough-to-b-wave peak, and the b/a-wave
228 ratio was calculated to normalize responses. OP amplitude was measured from trough-to-peak
229 of the largest wave and the OP/b-wave ratio was calculated using b-wave amplitudes from the
230 same recording.

231

232

233 *Patch clamp electrophysiology*

234 Retinas were isolated and embedded in 3% low melting point agarose (Sigma; Cat#
235 A0701) in carbogenated bicarbonate-buffered Ames medium (Ames & Nesbett, 1981; Ames
236 Medium w/L-Glutamate; US Biological; Swampscott, MA, USA; Cat# A1372-25) and 200-250 μm
237 slices were prepared with a Leica VT1200 vibrating microtome. For chemically simulated light
238 response experiments, retinas were sliced in carbogenated Ames. For all other recordings, slicing
239 was performed in chilled and carbogenated low-Na^+, high-sucrose cutting solution containing (in
240 mM): 210 sucrose, 35 $NaHCO_3$, 20 HEPES, 10 glucose, 6 $MgCl_2$, 3 sodium pyruvate, 2.5 KCl and
241 0.5 $CaCl_2$ and buffered to pH 7.4 with NaOH. Retina slices were stored at room temperature in
242 carbogenated Ames medium before being transferred to the recording chamber. Heated (31-33°
243 C) Ames medium was continuously perfused over the retinal slices during all patch-clamp
244 recordings.

245 Thick-walled borosilicate glass pipettes (World Precision Instruments; Sarasota, Fl, USA;
246 Cat# 1B150F-4) were pulled using a Narishige PP-830 electrode puller (Tokyo, Japan). Ultrapure
247 salts were purchased from Sigma-Aldrich (St. Louis, MO, USA). For RBC visualization, the
248 fluorescent tracer Alexa Fluor 594 Hydrazide (100 μM; Thermo Fisher Scientific; Cat# A10438)
249 was added to the pipettes. Whole-cell voltage-clamp and current-clamp recordings were
250 performed in photopic conditions using a double EPC-10 patch clamp amplifier controlled by
251 Patchmaster software (HEKA Elektronik, Lambrecht/Pfalz, Germany) or an Axon Axopatch 200B
252 controlled by pCLAMP software (Molecular Devices; San Jose, CA, USA). Data was acquired at
253 a 20 kHz sampling rate and filtered with a 2.9 kHz low-pass Bessel filter. RBCs were targeted
254 visually using Dodt gradient contrast microscopy and confirmed post-hoc with cell-filling and
255 epifluorescence microscopy. Both pCLAMP and Patchmaster data sets were exported to Igor Pro
256 (WaveMetrics, Lake Oswego, OR, USA) for offline analysis with custom Igor scripts and statistical
257 analysis was performed in Prism. We used a P/10 leak subtraction protocol (-80 mV to -73 mV)
258 in voltage-clamp to isolate voltage-gated Ca^{2+} currents and GABAergic feedback currents; leak
259 traces for each trial were baselined, summated, and subtracted from the raw pulse trace.

260 To record chemically simulated light responses, pipettes were pulled to 10-12 MΩ and
261 backfilled with a potassium gluconate solution containing (in mM): 125 K-gluconate, 8 KCl, 5
262 HEPES, 1 $MgCl_2$, 1 $CaCl_2$, 3 adenosine 5'-triphosphate magnesium salt (Mg-ATP), 0.5 guanosine
263 5'-triphosphate disodium salt (Na_2-GTP), and 5 EGTA, and pH was adjusted to 7.3 with KOH. The
264 Ames medium was supplemented with 4 μM L-(+)-2-amino-4-phosphonobutyric acid (L-AP4), an
265 mGluR6 agonist, to maintain a simulated dark-adapted state. A puffer pipette (12-18 MΩ) was
266 maneuvered into the dendritic field of the target cell, and the cell was patched in voltage-clamp

267 and held at -60 mV. The mGluR6 antagonist [RS]-α-cyclopropyl-4-phophophenylglycine (CPPG)
268 was applied directly to the dendrites using a Picospritzer II (Parker Hannifin; Hollis, NH, USA; 600
269 μM at 20 psi) for five seconds and the RBC response was recorded. For each cell, four sweeps
270 were recorded at 15-second intervals.

271 For current-clamp experiments, pipettes were pulled to 9-12 MΩ and backfilled with a
272 potassium gluconate solution containing (in mM): 104 K-gluconate, 10 KCl, 10 HEPES, 4 Mg-
273 ATP, 0.4 Na_2-GTP, 10 Na_2-Phosphocreatine, and 2 EGTA, and pH was adjusted to 7.3 with KOH.
274 The Ames medium was supplemented with 1 mM $CaCl_2$ and the synaptic blockers (in μM): 0.5
275 strychnine (glycine receptor blocker), 3 gabazine (SR 95531; $GABA_A$ receptor blocker), 50
276 [1,2,5,6-tetrahydropyridin-4-yl]methylphosphinic acid (TPMPA; $GABA_A\rho$ receptor blocker), and 4
277 L-AP4 to block excitatory and inhibitory inputs. The total external $CaCl_2$ concentration was
278 estimated to be 2.15 mM. Cells were first patched in voltage-clamp and then the amplifier was
279 switched to fast current-clamp mode using the EPC-10 Gentle CC-Switch feature. Resting
280 membrane voltage was recorded at 0 pA and then current was injected for 100 ms from -80 pA
281 to 80 pA in 20 pA steps. Peak voltage was measured as the peak (min or max) voltage
282 immediately after the onset of the current pulse, and sustained voltage was measured as the
283 average over the final 10 ms of the pulse. For each cell, five sets of sweeps were recorded at
284 five-second intervals.

285 For the remaining experiments, the pipettes were pulled to 5-8 MΩ and backfilled with a
286 cesium gluconate solution containing (in mM): 94 Cs-gluconate, 10 HEPES, 20 tetraethyl
287 ammonium chloride (TEA-Cl), 4 Mg-ATP, 0.4 Na_2-GTP, 10 Na_2-Phosphocreatine, and 2 EGTA,
288 and pH was adjusted to 7.3 with CsOH.

289 For voltage-clamp time-resolved capacitance recordings, the Ames medium was
290 supplemented with 1 mM $CaCl_2$ and (in μM): 0.5 strychnine, 3 gabazine, 50 TPMPA, and 4 L-AP4
291 to isolate voltage-gated Ca^{2+} currents and maximize membrane resistance. Pipettes were
292 wrapped with parafilm to reduce pipette capacitance and electrical noise. Membrane capacitance
293 (C_m), membrane resistance (R_m), and series resistance (R_s) were measured using the "sine + DC"
294 method implemented in Patchmaster software (Balakrishnan, Puthussery, Kim, Taylor, &
295 von Gersdorff, 2015; Gillis, 2000; Oltedal & Hartveit, 2010). Exocytosis was evoked in voltage-
296 clamp mode with a 100 ms depolarizing pulse from -80 mV to -10 mV to activate voltage-gated
297 Ca^{2+} currents. Resting C_m was measured using a sinusoidal voltage command (200 Hz, 30 mV
298 trough-to-peak) superimposed over the membrane holding potential (-80 mV) and one
299 measurement was generated per cycle (**Figure 5A**). An increase in exocytosis (ΔC_m) was

300 measured from the change in C_m values before and after the depolarizing pulse. A baseline was
301 established by averaging the resting C_m over the one second immediately preceding the voltage
302 step. C_m measurements immediately after repolarization were excluded from analysis to allow for
303 the full decay of evoked conductances and C_m was averaged over the following 500 ms. Cells
304 were discarded if changes in C_m correlated significantly with changes in R_m or R_s. For each cell,
305 five sets of sweeps were recorded with 15 second intervals. To remove noise, C_m data was filtered
306 through a 5 Hz low-pass FIR filter. When different frequency sinusoidal voltage commands were
307 used, recordings were resampled to 200 Hz for ease of comparisons.
308 To record reciprocal inhibitory currents, the Ames medium was supplemented with 1 mM
309 $CaCl_2$, 4 μM L-AP4, and 0.5 μM strychnine. Feedback current was evoked in voltage-clamp mode
310 with a 100 ms depolarizing pulse from -80 mV to -10 mV to activate voltage-gated Ca^{2+} currents
311 and subsequent outward GABAergic inhibitory currents. We isolated inhibitory currents (I_{Inhib}) by
312 subtracting recordings with GABA blockers (I_{Ca}) were from recordings without GABA blockers
313 (I_{Total}), and calculated the charge transfer across the duration of the depolarizing pulse. Five sets
314 of sweeps were recorded at five-second intervals.
315
316 **Results**
317 *TPBG is not required for normal gross RBC morphology*
318 We used the constitutive Tpbg knockout mouse line B6;129S5-Tpbg^{tm1Lex}/Mmucd (referred
319 to as TPBG-KO or KO) to analyze the consequences of genetic deletion of TPBG in the retina.
320 Wild type (WT) littermates were used as controls. Expression and localization of TPBG were
321 examined by western blotting and immunofluorescence confocal microscopy (**Figure 1**). As
322 previously reported (Wakeham et al., 2020), the TPBG antibody labels RBC cell bodies, dendrites,
323 and axon terminals in the WT retina, as well as a narrow band in the middle of the IPL
324 corresponding to the processes of TPBG-expressing amacrine cells. TPBG immunoreactivity was
325 absent throughout the KO retina (**Figure 1A**); this was confirmed by immunoblotting (**Figure 1B**)
326 of WT and KO retinal lysates with the TPBG antibody using β-actin as a loading control. Using
327 an antibody against PKCα in WT and TPBG-KO retina, we found no discernable disruption in
328 morphology of RBC dendrites or axon terminals in KO retinas (**Figure 1C-D**).

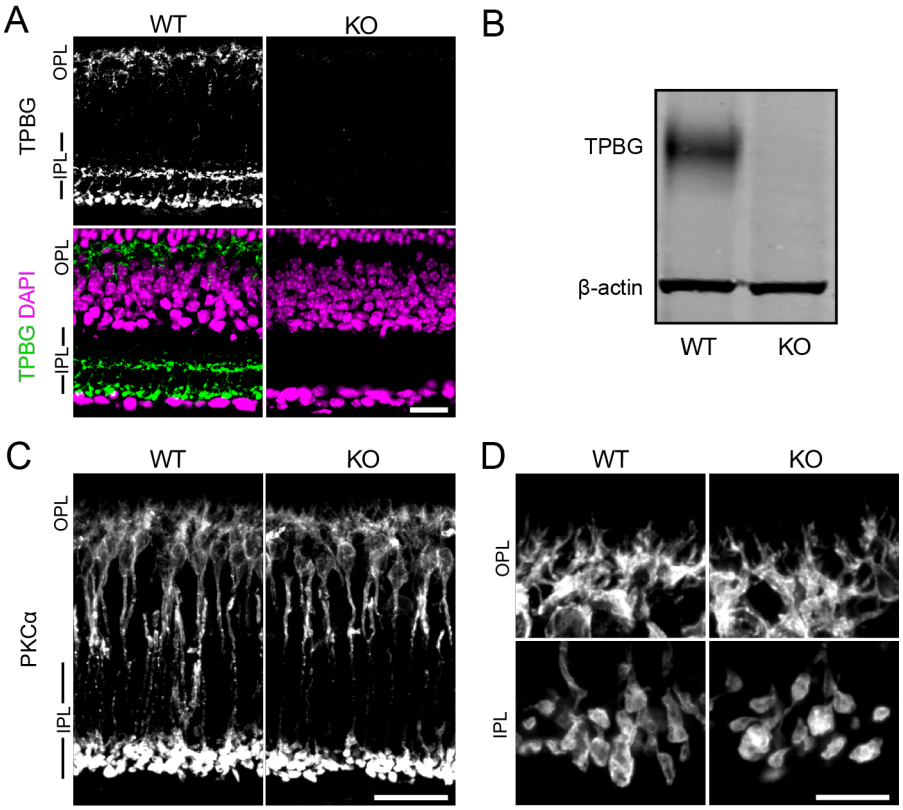

Figure 1: TPBG-KO does not alter gross RBC morphology. **(A)** Immunofluorescence confocal microscopy of WT (left) and TPBG-KO (KO; right) retina sections labeled with an antibody against TPBG (green). The nuclear stain DAPI (bottom; magenta) was used to highlight the neuronal layers of the retina. **(B)** Immunoblot of WT and TPBG-KO (KO) retinal lysates probed for TPBG and β-actin. The two channels were imaged separately and merged. **(C)** Confocal microscopy of WT (left) and TPBG-KO (KO; right) retina sections labeled with an antibody against PKCα. **(D)** Close-up images depicting the OPL (top) and IPL (bottom) for better visualization. For all images, Z-projections of 11 sections were used with a Z-step distance of 0.415 μm for a total thickness of 4.57 μm. Intensity and contrast was adjusted equally across genotypes. OPL: outer plexiform layer; IPL: inner plexiform layer. Scale bars: **(A and C)** 20 μm; **(D)** 10 μm.

Genetic knockout of TPBG alters the scotopic ERG light response

The light response of RBCs is reflected in the b-wave of the dark-adapted (scotopic) full-field electroretinogram (ERG), a commonly-used technique for recording the electrical responses of the whole retina *in vivo*. Different components of the ERG waveform correspond to the activity of specific cell types in the retina. The a-wave is an initial negative deflection corresponding to hyperpolarization of the photoreceptors (Robson & Frishman, 2014), whereas the b-wave, a larger and slower positive deflection, primarily corresponds to the subsequent depolarization of the ON-bipolar cells (Stockton & Slaughter, 1989). Rod driven activity can be isolated by dark-adapting the mouse before testing; therefore, the dark-adapted ERG b-wave represents the activity of RBCs in response to light stimuli.

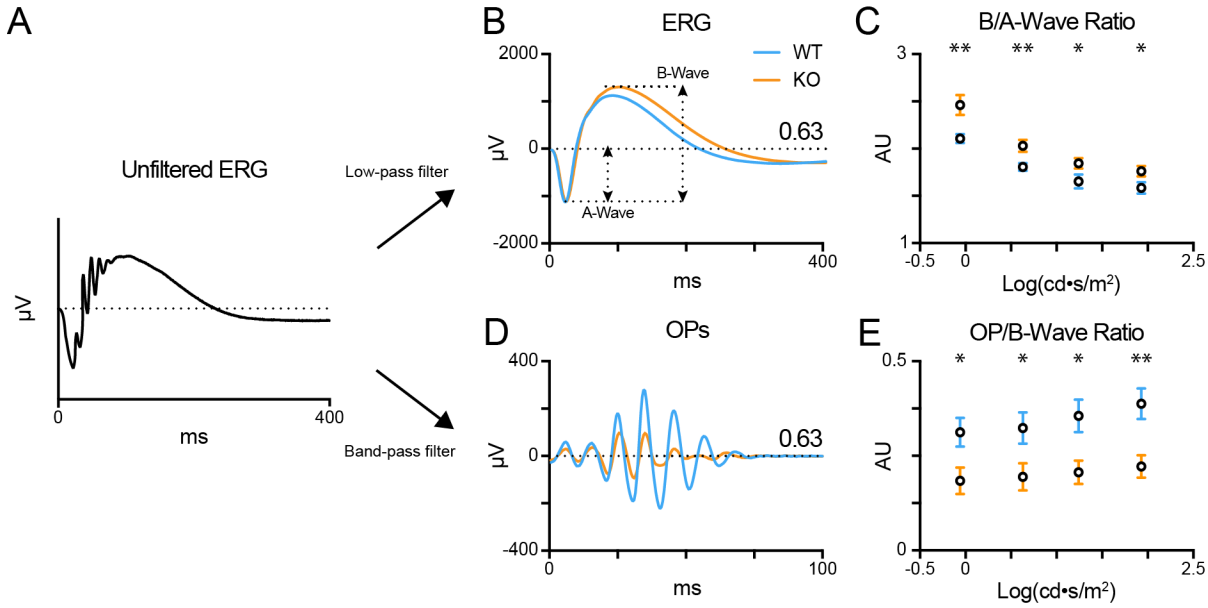

Figure 2: TPBG-KO alters the scotopic ERG after bright stimuli. Scotopic electroretinograms (ERGs) were recorded from dark-adapted WT (blue; n = 12) and TPBG-KO (KO; orange; n = 14) mice after light stimuli (-0.06 to 1.93 log(cd•s/m^2)). **(A)** After baselining the raw, unfiltered ERG traces, a 60 Hz low-pass filter was used to remove OPs to better visualize the a- and b-waves. A 30-300 Hz Butteworth band-pass filter was used to isolate OPs from the ERG for quantification. **(B)** Average ERG recordings after light stimuli of 0.63 log(cd•s/m^2). A-wave amplitudes were measured from baseline to the a-wave trough and b-wave amplitudes were measured from the a-wave trough to the b-wave peak. **(C)** Quantification of b-wave amplitudes normalized to a-wave amplitudes. **(D)** Average oscillatory potentials (OPs) after light stimuli of 0.63 log(cd•s/m^2). **(E)** Quantification of OP amplitudes normalized to b-wave amplitudes. OP amplitudes were measured from the trough to peak of the largest wave. Quantified data is presented as the mean ± SEM. Statistical significance was determined using Welch's t-tests; ns: $p > 0.05$; *: $p < 0.05$; ** $p < 0.01$.

We recorded the scotopic ERG light responses in dark-adapted anesthetized WT (blue; n = 12) and TPBG-KO (KO; orange; n = 14) mice across several stimulus intensities, from dim (-0.06 log(cd•s/m^2)) to bright (1.93 log(cd•s/m^2)). We applied a 60 Hz low-pass filter to remove oscillatory potential (OP) contamination from the ERG a- and b-waves, and a 30-300 Hz Butterworth band-pass filter to isolate OPs for further analysis (**Figure 2A**). There was no difference in a-wave amplitudes across intensities (**Figure 2: Supplementary Figure**), indicating that the KO did not affect the rod photoreceptor light responses, but there was an enlarged b-wave in the TPBG-KO mouse (**Figure 2B**). Because the ERG b-wave is dependent on upstream photoreceptor activation, which is represented by the a-wave, it is common practice for ERG b-wave amplitudes to be normalized to a-wave amplitudes for comparison across animals. The TPBG-KO increased the normalized b-waves (b/a-wave ratio) across the range of stimuli intensities (**Figure 2C**), indicating a larger and more prolonged RBC light response in TPBG-KO mice.

Oscillatory potentials (OPs) are low amplitude, high frequency waves superimposed over the rising phase of the ERG b-wave and observed after bright stimuli. Previous studies indicate

377 that OPs originate from rhythmic activity in the IPL downstream of the bipolar cells (Ogden, 1973).
378 Because the light response of a dark-adapted retina is primarily rod-driven, the OPs are indirectly
379 correlated to RBC output. Therefore, we normalized the OP amplitude by the b-wave amplitude
380 (OP/b-wave ratio) of the corresponding ERG recording. Normalized TPBG-KO OPs were reduced
381 compared to WT (**Figure 2D and E**). TPBG is primarily expressed in RBCs, therefore an effect of
382 TPBG-KO on the OPs is most likely to be due to reduced RBC output onto downstream neurons,
383 though an effect mediated by the TPBG-expressing amacrine cells cannot be ruled out.

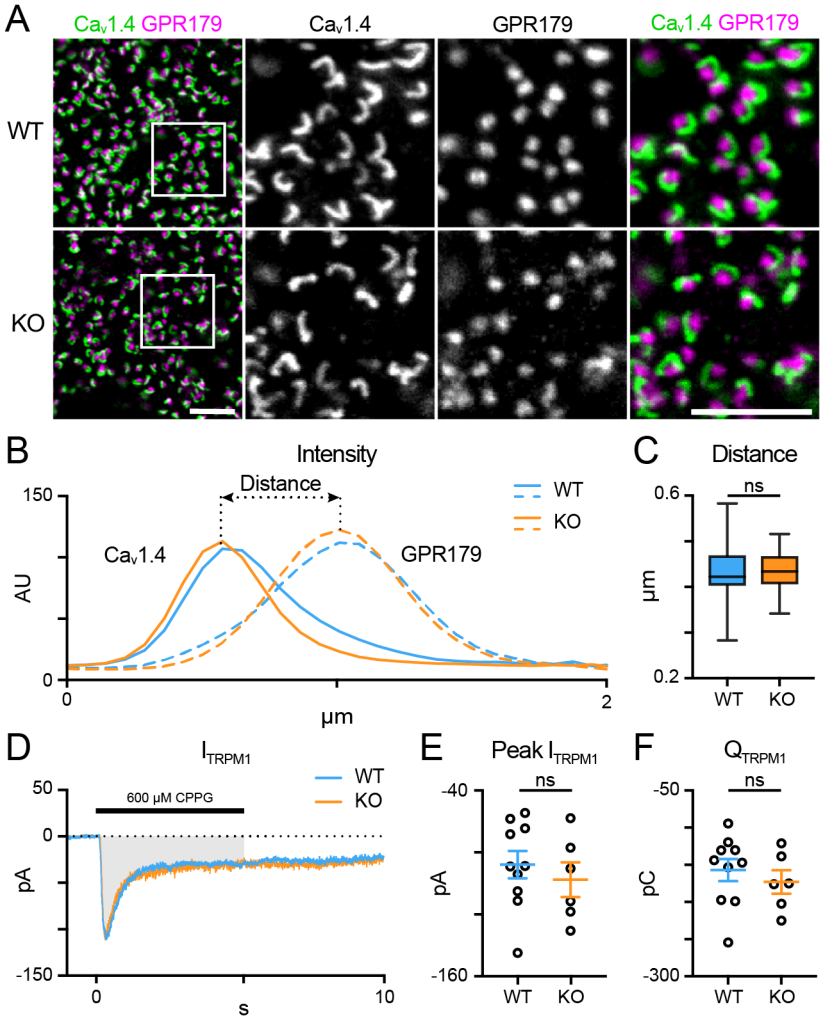

384

385 ***Figure 3: TPBG is not required for mGluR6-driven responses in RBC dendrites***. (**A**) Immunofluorescence confocal
386 microscopy from WT and TPBG-KO whole mount retinas using antibodies against the rod presynaptic calcium channel
387 $Ca_v1.4$ (green) and the RBC post-synaptic protein GPR179 (magenta). Square boxes in the leftmost images indicate
388 regions of interest expanded in the other images. Z-projections of two sections were used with a Z-step distance of
389 0.297 µm for a total thickness of 0.594 µm. Scale bar is 5 µm. **(B)** Plot of fluorescence intensity over distance from
390 $Ca_v1.4$ (left) and GPR179 (right) channels from WT (blue; *n* = 66 synapses) and TPBG-KO (KO; orange; *n* = 54
391 synapses). **(C)** Quantification of synaptic distance. Box plot extends from the first to the third quartile and the whiskers
392 extend across all points. The line in the box represents the median. **(D-F)** Chemically simulated light responses were
393 recorded in WT (blue; *n* = 10) and TPBG-KO (KO; orange; *n* = 6) RBCs following a pulse of 600 µM CPPG for 5

seconds. **(D)** Example CPPG-induced TRPM1 currents. The gray bar represents the region across which charge transfer was calculated. **(E)** Quantification of peak CPPG-induced TRPM1 current (I_{TRPM1}) and **(F)** charge transfer (Q_{TRPM1}) over the five-second duration of the CPPG pulse. For **E** and **F**, open circles represent single cells and colored bars represent the mean ± SEM. Statistical significance was determined using Welch's *t*-tests; ns: $p > 0.05$.

TPBG is not required for mGluR6-driven responses in RBC dendrites

We examined the expression and localization patterns of key pre- and post-synaptic proteins that are required for synaptic transmission between rod photoreceptors and RBCs. RBCs receive synaptic input from rod photoreceptors via a sign-inverting signal transduction cascade localized to the tips of RBC dendrites. Glutamate released from rod photoreceptors is detected by the group III metabotropic glutamate receptor mGluR6 (Masu et al., 1995; Nakajima et al., 1993; Vardi, Duvoisin, Wu, & Sterling, 2000; Xu et al., 2012), that is negatively coupled to the TRPM1 cation channel (Koike, Numata, Ueda, Mori, & Furukawa, 2010; Koike, Obara, et al., 2010; Morgans et al., 2009; Shen et al., 2009). Thus, a light stimulus relieves TRPM1 tonic inhibition, permitting cation influx and subsequent RBC depolarization.

First, we looked at the spatial relationship between presynaptic elements in the rod spherule and the tips of the RBC dendrites (**Figure 3A**) using an antibody against the rod L-type Ca^{2+} channel subunit $Ca_v1.4$ to label the horseshoe-shaped active zone and an antibody that labels GPR179 in RBC dendritic tips (Hasan, Ray, & Gregg, 2016). In normal rod-RBC synapses, GPR179 labeling appears as puncta within the concavity of the horseshoe-shaped $Ca_v1.4$ immunofluorescence. We quantified the spatial relationship between rod active zones and RBC dendritic tips by measuring the distance between the peak intensity for each fluorescent channel (**Figure 3B**). We found no difference between WT (blue; $n = 66$ synapses from eight animals) and TPBG-KO (KO; orange; $n = 54$ synapses from seven animals) synaptic distance (**Figure 3C**; WT: 0.43 ± 0.006 μm; KO: 0.43 ± 0.004 μm; Welch's *t*-test: $p = 0.96$, $t(117.60) = 0.052$), suggesting that RBC dendrites form morphologically normal invaginations into rod spherules in the TPBG-KO mouse.

Scotopic ERG recordings revealed increased b-waves in TPBG-KO mice (**Figure 2**) indicating an enhanced light response in KO RBCs. Because the RBC light response is initiated by TRPM1, we compared TRPM1 currents between WT (blue; $n = 10$) and TPBG-KO (KO; orange; $n = 6$) RBCs by recording chemically simulated light responses in retinal slices in whole-cell voltage-clamp (**Figure 3D-F**). In this technique, bath application of the mGluR6 agonist L-AP4 maintains the retina in a simulated dark-adapted state, and brief puffs of the mGluR6 antagonist, CPPG, onto the dendrites simulates a light flash and evokes TRPM1 currents (**Figure 3D**). TPBG-KO did not alter the CPPG-induced TRPM1 peak current (**Figure 3E**; WT: -88.24 ± 8.92 pA; KO: -98.04 ± 11.28 pA; Welch's *t*-test: $p = 0.51$, $t(10.85) = 0.68$) or charge transfer

430 (**Figure 3F**; WT: -157.10 ± 47.01 pC; KO: -173.10 ± 38.62 pC; Welch's *t*-test: $p = 0.47$, $t(12.40) =$
431 0.74). These results suggest that TPBG is not required for the formation of functional rod-RBC
432 synapses and that the larger scotopic ERG b-waves do not reflect enhanced TRPM1 currents in
433 the TPBG-KO.
434
435 *Synaptic ribbons are smaller in TPBG-KO RBCs compared to WT*
436 Oscillatory potentials are thought to be generated by the inner retina, and RBCs drive the
437 majority of downstream activity under scotopic conditions; thus, the attenuation of scotopic OPs
438 in the TPBG-KO suggests a deficit in RBC output to third-order neurons. Like rods, RBCs signal
439 to downstream cells using ribbon synapses. A depolarized potential entering the axon terminal
440 prompts the opening of L-type voltage-gated Ca^{2+} channels clustered beneath the ribbons and
441 the resulting influx of Ca^{2+} triggers the fusion (exocytosis) of ribbon-tethered synaptic vesicles
442 (Gersdorff, Vardi, Matthews, & Sterling, 1996). This process requires a close spatial relationship
443 between the Ca^{2+} channels the synaptic ribbons (Jarsky, Tian, & Singer, 2010). We used triple
444 immunofluorescence microscopy to examine the relative localization and expression patterns of
445 the L-type Ca^{2+} channel subunit, $Ca_v1.4$, and the primary structural synaptic ribbon protein
446 RIBEYE (**Figure 4A-C**). Because neither $Ca_v1.4$ nor RIBEYE are specific to RBC axon terminals,
447 we isolated RBC-specific immunofluorescence using a binary mask derived from PKCα
448 immunofluorescence to exclude labeling from other bipolar cells in the IPL. $Ca_v1.4$ and RIBEYE
449 show punctate immunofluorescence in RBC axon terminals and are co-localized or closely
450 apposed (**Figure 4A**). Mander's coefficients (M1 and M2) were calculated to examine
451 colocalization between $Ca_v1.4$ and RIBEYE puncta in both control (PKCα-negative) terminals and
452 RBC (PKCα-positive) terminals (**Figure 4B**). We found no differences in co-localization
453 coefficients between WT and TPBG-KO control or RBC axon terminals: WT (blue; $n = 134$ control
454 puncta and 100 RBC puncta) and TPBG-KO (orange; $n = 327$ control puncta and 119 RBC
455 puncta), control M1 (WT: 0.53 ± 0.022 arbitrary units (AU); KO: 0.52 ± 0.013 AU; Welch's *t*-test:
456 $p = 0.60$, $t(237.2) = 0.53$), control M2 (WT: 0.40 ± 0.015 AU; KO: 0.42 ± 0.011 AU; Welch's *t*-test:
457 $p = 0.28$, $t(288.1) = 1.09$), RBC M1 (WT: 0.66 ± 0.016 AU; KO: 0.64 ± 0.015 AU; Welch's *t*-test: p
458 $= 0.47$, $t(208.3) = 0.73$), RBC M2 (WT: 0.32 ± 0.01 AU; KO: 0.31 ± 0.01 AU; Welch's *t*-test: $p =$
459 0.76, $t(216.9) = 0.31$). Additionally, we found that the number of ribeye puncta per unit area was
460 unchanged in WT (blue; $n = 90$ axon terminals) and TPBG-KO (KO; orange; $n = 109$ axon
461 terminals) RBC terminals (**Figure 4C**; WT: 2.07 ± 0.66 puncta/μm^2; KO: 2.03 ± 0.58 puncta/μm^2;
462 Welch's *t*-test: $p = 0.70$, $t(177.8) = 3.92$). We also compared synaptotagmin I/II

463 immunofluorescence between RBC axon terminals in WT and TPBG-KO retinas and saw no
464 difference (not shown; WT: 1.352 ± 0.0486 AU; KO: 1.446 ± 0.0560; Welch's t-test: p-value =
465 0.209, t(52.63) = 1.271).
466

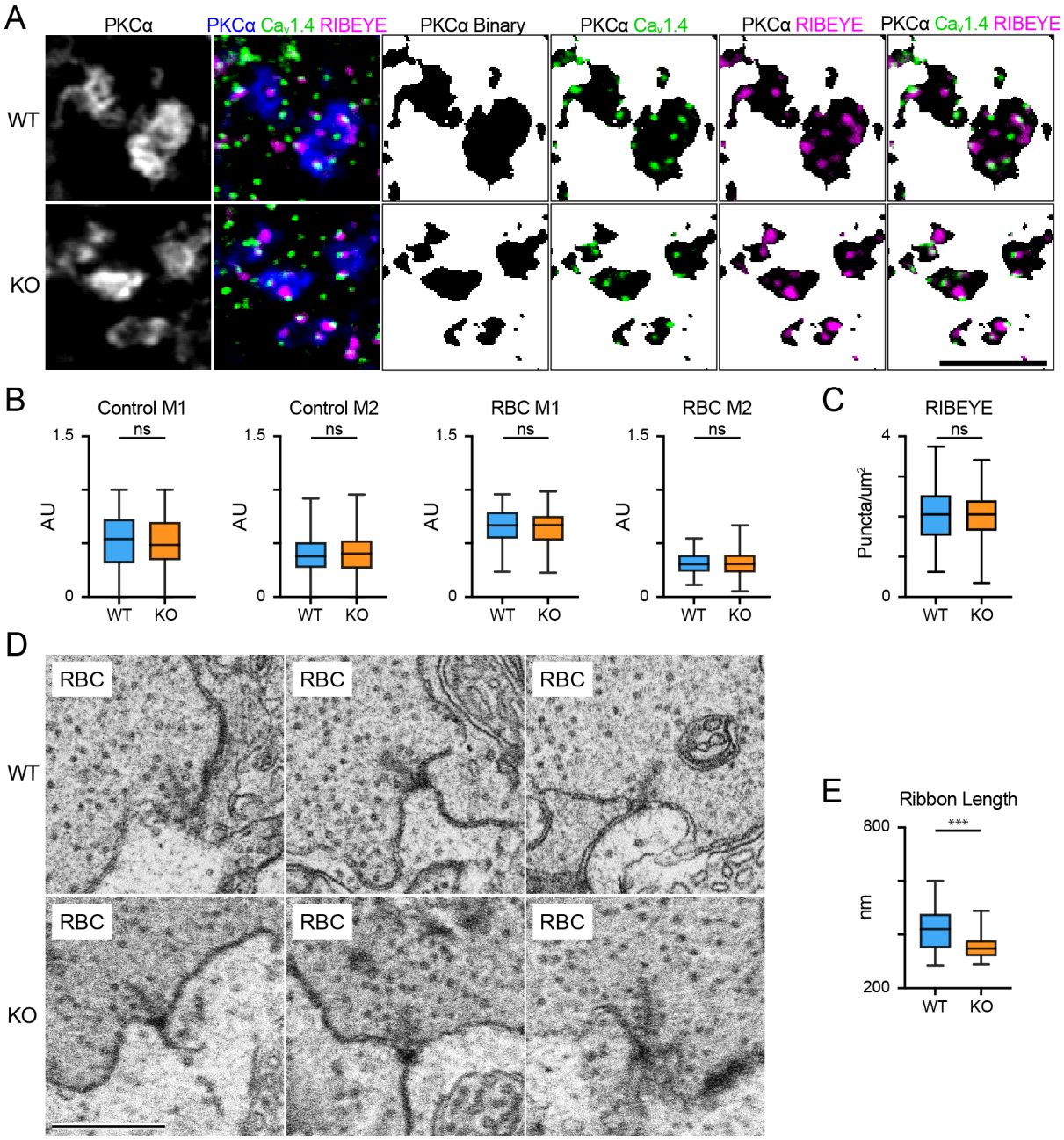

467

468 ***Figure 4: RBC synaptic ribbons are smaller in the TPBG-KO retina.*** (**A**) Triple immunofluorescence confocal
469 microscopy of WT and TPBG-KO (KO) whole mount retinas using antibodies against PKCα (blue), $Ca_v1.4$ (Green) and
470 RIBEYE (magenta). To isolate labeling in RBC axon terminals, binary images were created using the PKCα channel
471 and overlayed over the other two channels to generate binary masks. Z-projections of two sections were used with a
472 Z-step distance of 0.297 μm for a total thickness of 0.547 μm. The scale bar is 5 μm. (**B**) Quantification of $Ca_v1.4$ and
473 RIBEYE colocalization in WT (blue) and TPBG-KO (KO; orange) using M1 and M2 Mander's coefficients in control
474 (WT: *n* = 134 puncta; KO: *n* = 327 puncta) and RBC axon terminals (WT: *n* = 100 puncta; KO: *n* = 119 puncta). (**C**)

Quantification of RIBEYE puncta counts in WT (blue; *n* = 90 terminals) and TPBG-KO (KO; orange; *n* = 109 terminals). (**D**) Example FIB-SEM images showing RBC active zones from WT (top) and TPBG-KO (KO; bottom) RBC axon terminals. Scale bar is 500 nm. (**E**) Quantification of synaptic ribbon length in WT (blue; *n* = 33 ribbons) and TPBG-KO (KO; orange; *n* = 38 ribbons) measured from the membrane. Box plots extend from the first to the third quartile and the whiskers extend across all points. The line in the box represents the median.

To examine synaptic ribbons in RBC axon terminals, serial electron micrographs were collected from a volume each of WT and TPBG-KO retina using a focused ion beam scanning electron microscope (FIB-SEM). Bipolar cell terminals closest to the ganglion cell layer were identified as putative RBC axon terminals. The general ultrastructure of the RBC axon terminals, including the synaptic vesicles, synaptic ribbons, and postsynaptic elements was similar in WT and TPBG-KO retina. To estimate synaptic ribbon size, we measured the maximum distance that each ribbon extended into the cytoplasm from its attachment site on the plasma membrane in WT (blue; *n* = 33 ribbons) and TPBG-KO (KO; orange; *n* = 38 ribbons) and found that synaptic ribbons were 15% smaller in TPBG-KO RBCs compared to WT RBCs (**Figure 4E**; WT: 416.8 $\pm$ 13.78 nm; KO: 355.7 $\pm$ 8.85 nm; Welch's *t*-test: $p = 0.0004$, $t(55.65) = 3.74$).

TPBG is required for efficient exocytosis in RBC synaptic terminals.

To examine the effect of TPBG-KO on RBC synaptic output, we recorded time-resolved membrane capacitance (C_m) before and after a depolarizing pulse using the "sine + DC" method (Gillis, 2000; Oltedal & Hartveit, 2010). High-resolution membrane capacitance changes (ΔC_m) after a depolarizing pulse strongly correlate with vesicle exocytosis in neuroendocrine cells (Klyachko & Jackson, 2002; Neher & Marty, 1982) and glutamate release from bipolar cell axon terminals (Kim & von Gersdorff, 2016). A sinusoidal voltage command (200 Hz at 30 mV trough-to-peak) was superimposed over the holding voltage of -80 mV and exocytosis was evoked by depolarizing the cell to -10 mV to open the voltage-gated Ca^{2+} channels (**Figure 5: Supplementary Figure A)**. Membrane capacitance (C_m), membrane resistance (R_m), and series resistance (R_s) were recorded before and after the pulse and ΔC_m was measured as the change in C_m after exocytosis. Changes in R_m and R_s were not correlated with changes in C_m (**Figure 5: Supplementary Figure B**).

C_m measurements in RBCs are complicated by the attenuation and filtering of the sinusoidal voltage command amplitude down their narrow axons (Oltedal & Hartveit, 2010; Oltedal, Veruki, & Hartveit, 2009). We sought to confirm that a low-frequency sinusoidal command reduces attenuation and maximizes RBC C_m changes compared to higher frequencies (**Figure 5: Supplementary Figure C-F**) using 200 (n = 6), 400 (n = 4), 800 (n = 4), and 1600 (n = 4) Hz commands. We found no difference in the voltage-gated Ca^{2+} current amplitude (I_{Ca}) or charge

transfer (Q_{Ca}) across frequencies (not shown), but the ΔC_m (**Figure 5: Supplementary Figure C-D**; 200 Hz: 41.94 ± 4.95 fF; 400 Hz: 19.13 ± 4.06 fF; 800 Hz: 4.05 ± 2.91 fF; 1600 Hz: -4.23 ± 1.40; Brown-Forsythe ANOVA: $p < 0.0001$, 34.12(2.00, 10.87)) and the resting C_m (**Figure 5: Supplementary Figure E-F**; 200 Hz: 5.97 ± 0.23 pF, 400 Hz: 5.73 ± 0.12 pF, 800 Hz: 4.81 ± 0.15 pF, 1600 Hz: 4.04 ± 0.12 pF; Brown-Forsythe ANOVA: $p < 0.0001$, 25.06(3.00, 11.34)) were greater at 200 Hz compared to higher frequencies. These supplementary results support our decision to examine exocytosis in RBCs using a 200 Hz "sine + DC" protocol.

To examine RBC synaptic vesicle exocytosis, we used whole-cell voltage-clamp to compare WT (blue; n = 6) and TPBG-KO (KO; orange; n = 7) voltage-gated Ca^{2+} currents and subsequent changes in membrane capacitance (**Figure 5**). Cells where C_m, R_m, and R_s were highly correlated were discarded. The synaptic blockers L-AP4, strychnine, TPMPA, and gabazine were used to block spontaneous activity and help increase and stabilize R_m during recordings. The passive properties of R_m (WT: 1.603 ± 0.24 GΩ; KO: 1.630 ± 0.16 GΩ; Welch's *t*-test: $p = 0.93$, $t(8.84) = 0.097$) and R_s (WT: 50.54 ± 2.33 MΩ; KO: 49.61 ± 1.91 MΩ; Welch's *t*-test: $p = 0.76$, $t(10.16) = 0.31$) were not different between WT and TPBG-KO RBCs. As long as R_m is significantly greater than R_s, ΔC_m should be a faithful approximation of overall exocytosis (Gillis, 2000).

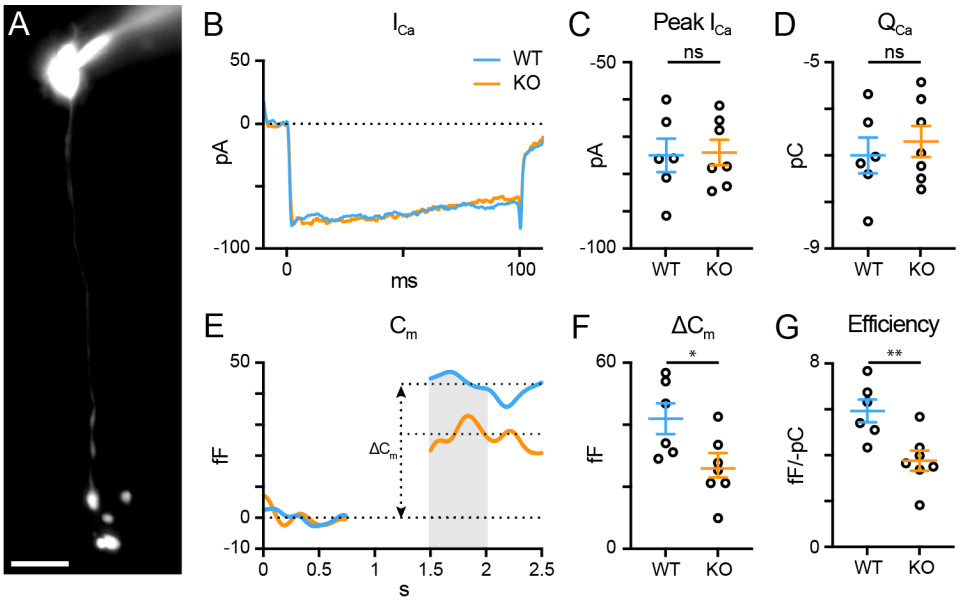

Figure 5: TPBG is required for efficient synaptic vesicle release in RBC axon terminals. Whole-cell voltage-clamp recordings were performed in WT (blue; *n* = 6) and TPBG-KO (KO; orange; *n* = 7) RBCs. **(A)** Epifluorescence micrograph of an RBC filled with Alexa Fluor 594 Hydrazide after patch-clamp recording. RBCs were patched and cell type was verified *post-hoc* using epifluorescence microscopy. The scale bar is 10 μm. **(B)** Average voltage-gated Ca^{2+} current traces recorded after a depolarizing pulse from -80 mV to -10 mV for 100 ms. **(C)** Quantification of peak voltage-gated Ca^{2+} current amplitudes (I_{Ca}) and **(D)** charge transfer (Q_{Ca}) over the duration of the pulse. **(E)** Average membrane capacitance (C_m) recordings using a 200 Hz sine + DC protocol. ΔC_m was measured as the difference between baselined resting C_m before and after the depolarizing pulse. Data immediately after the pulse was excluded until C_m

stabilized. The gray bar represents the region across which C_m values were averaged. **(F)** Quantification of ΔC_m. **(G)** Quantification of exocytosis efficiency calculated as the absolute value of the change in C_m per unit Q_{Ca}. Ames medium was supplemented with 1 mM $CaCl_2$ and (in μM): 0.5 strychnine, 3 gabazine, 50 TPMPA, and 4 L-AP4. Open circles in bar graphs represent single cells and bars represent the mean ± SEM. Statistical significance was determined using Welch's *t*-tests; ns: $p > 0.05$; *: $p < 0.05$; **: $p < 0.01$.

TPBG-KO had no effect on the voltage-gated Ca^{2+} currents (**Figure 5B-C**; WT: -74.99 ± 4.49 pA, KO: -74.24 ± 3.41 pA; Welch's *t*-test: $p = 0.90$, $t(9.73) = 0.13$) or charge transfer (**Figure 5D**; WT: -7.0 ± 0.38 pC, KO: -6.7 ± 0.33 pC; Welch's *t*-test: $p = 0.57$, $t(10.43) = 0.58$). However, TPBG-KO resulted in a reduction in ΔC_m compared to WT (**Figure 5E-F**; WT: 41.94 ± 4.95 fF, KO: 25.90 ± 3.91 fF; Welch's *t*-test: $p = 0.029$, $t(9.95) = 2.55$), suggesting a decrease in synaptic vesicle exocytosis in the KO. Most interestingly, the efficiency of exocytosis (the ratio of ΔC_m per unit Q_{Ca}) is also reduced in the KO (**Figure 5G**; WT: 5.93 ± 0.50 fF/-pC, KO: 3.76 ± 0.44 fF/-pC; Welch's *t*-test: $p = 0.0077$, $t(10.52) = 3.28$), indicating that TPBG-KO alters the efficiency of RBC vesicle exocytosis without changing Ca^{2+} influx.

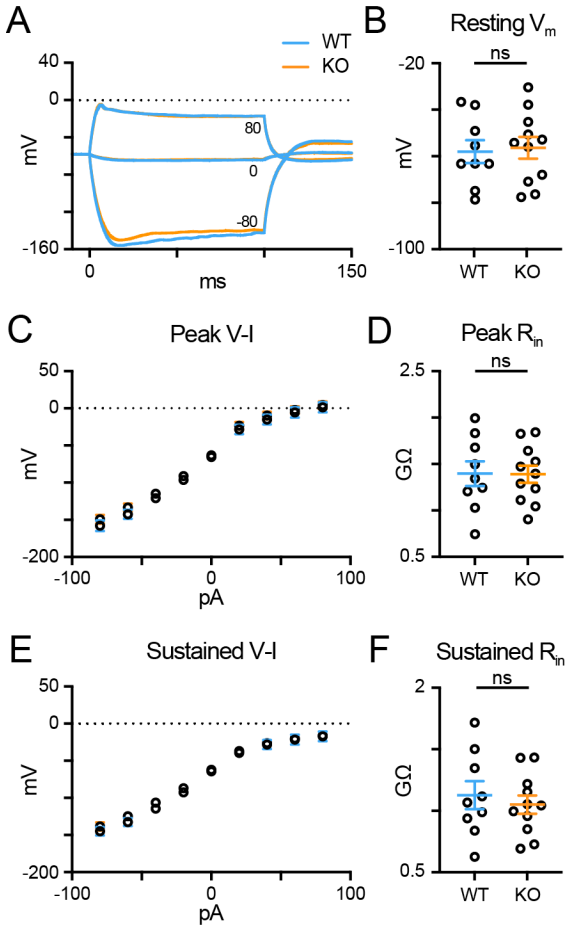

Figure 6: TPBG does not alter RBC input resistance or excitability. Whole-cell current-clamp recordings in WT (blue; $n = 9$) and TPBG-KO (KO; orange; $n = 11$) RBCs were used to construct a current-voltage relationship and calculate input resistance (R_{in}). A current injection protocol from -80 pA to 80 pA in 20 pA steps was used with a K-gluconate-based internal solution. **(A)** Average voltage traces following -80 pA, 0 pA, and 80 pA current injections for 100 ms. **(B)** Resting membrane voltages recorded immediately after entering current clamp mode. **(C)** A plot of the voltage-current (V-I) relationship measured at the peak voltage during current injections. **(D)** Quantification of peak R_{in}.

558 **(E)** A plot of the sustained V-I relationship measured as the average voltage calculated over the last 10 ms of the
559 current pulse. **(F)** Quantification of the sustained R_{in}. Peak and sustained R_{in} values were calculated by measuring the
560 slope of the linear portion of the V-I curves (from -40 to 40 pA). Ames medium was supplemented with 1 mM $CaCl_2$
561 and (in μM): 0.5 strychnine, 3 gabazine, 50 TPMPA, and 4 L-AP4. For V-I curves, open circles represent the mean and
562 error bars represent SEM. For quantification, open circles represent single cells and bars represent the mean ± SEM.
563 Statistical significance was determined using Welch's *t*-tests; ns: $p > 0.05$.
564

565 *TPBG does not alter RBC input resistance or excitability*

566 TPBG-KO amplifies the RBC light response and reduces synaptic vesicle exocytosis,
567 suggesting that TPBG-KO may reduce the gain of RBC synaptic release by shifting RBC
568 excitability. To compare the excitability between WT (blue; $n = 9$) and TPBG-KO (KO; orange; n
569 $= 11$) RBCs, we used current injections (from -80 to 80 pA in 20 pA intervals) in whole-cell current-
570 clamp mode to construct voltage-current relationships and calculate the peak and sustained input
571 resistances (R_{in}). For these experiments, we used the synaptic blockers L-AP4, strychnine,
572 TPMPA, and gabazine to isolate RBC-specific voltage responses. **Figure 6A** shows voltage
573 responses after representative current injections of -80 pA, 0 pA, and +80 pA. The resting
574 membrane potential (V_m) was unchanged in the KO (**Figure 6B**; WT: -58.02 ± 4.91 mV, KO: -
575 56.35 ± 4.66 mV; Welch's *t*-test: $p = 0.81$, $t(17.53) = 0.25$). We found no difference in peak (**Figure**
576 **6C-D**; WT: 1.40 ± 0.13 GΩ, KO: 1.39 ± 0.09 GΩ; Welch's *t*-test: $p = 0.97$, $t(14.94) = 0.04$) or
577 sustained R_{in} (**Figure 6E-F**; WT: 1.13 ± 0.11 GΩ, KO: 1.05 ± 0.07 GΩ; Welch's *t*-test: $p = 0.58$,
578 $t(14.28) = 0.56$) between the WT and KO RBCs. These results indicate that a shift in R_{in} and RBC
579 excitability in the TPBG-KO do not explain the reduced exocytosis.
580

581 *TPBG-KO reduces reciprocal inhibitory feedback*

582 RBCs drive retinal output via glutamate release into the IPL, which stimulates Ca^{2+}-
583 permeable AMPA receptors in downstream AII amacrine cells (AII-ACs). RBC glutamate release
584 is also detected by A17 amacrine cells (A17-ACs), which when depolarized, release GABA back
585 onto RBC synaptic terminals where it is sensed by $GABA_A$ and $GABA_A\rho$ (also called $GABA_C$) Cl^-
586 channels (**Figure 7A**). An influx of Cl^- into the axon terminal through open GABA channels
587 provides inhibitory feedback by hyperpolarizing the RBC and shaping further RBC glutamate
588 release (Chávez, Grimes, & Diamond, 2010; Chávez, Singer, & Diamond, 2006; Euler & Masland,
589 2000; E. Hartveit, 1996; Espen Hartveit, 1999; Singer & Diamond, 2003). Each RBC active zone
590 forms a dyad synapse with one AII-AC and one A17-AC (Famiglietti & Kolb, 1975; Grimes, Zhang,
591 Graydon, Kachar, & Diamond, 2010; McGuire, Stevens, & Sterling, 1984; Raviola & Dacheux,
592 1987). As A17-mediated reciprocal feedback is driven by RBC glutamate release, the inhibitory

feedback currents in the RBCs are an indirect measure of glutamate release from RBCs and would be expected to be reduced concomitantly with reduced RBC exocytosis in the TPBG-KO.

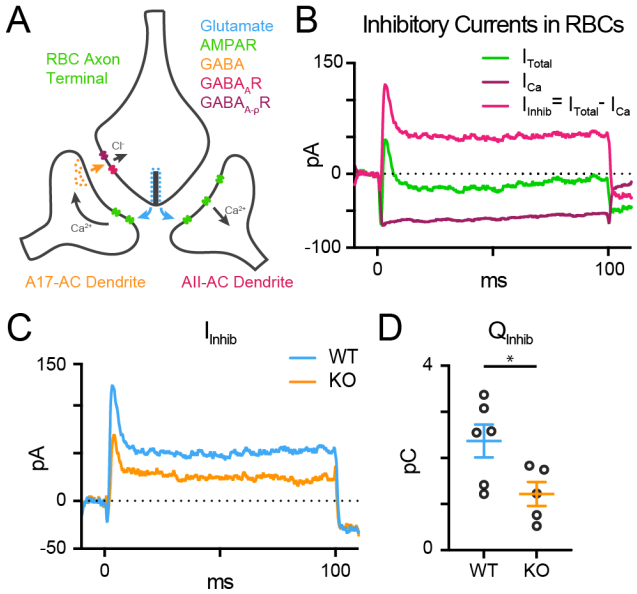

Figure 7: TPBG-KO reduces reciprocal inhibitory feedback. **(A)** The dyad synapse arrangement between one RBC, one AII-AC, and one A17-AC in the IPL. Glutamate release by RBCs is detected by Ca^{2+}-permeable AMPA receptors (AMPARs) in AII-AC and A17-AC dendrites. A17-ACs then release GABA back onto the synaptic cleft which is sensed by $GABA_A$ receptors ($GABA_A$Rs) and $GABA_{A\rho}$ receptors ($GABA_{A\rho}$Rs) in the RBC axon terminals. **(B)** Inhibitory currents are superimposed over voltage-gated Ca^{2+} currents. Reciprocal feedback in RBCs was evoked with a 100 ms depolarizing pulse from -80 mV to -10 mV. In the absence of GABA receptor blockers, this depolarizing pulse elicits an inward voltage-gated Ca^{2+} current that is quickly subsumed by outward inhibitory currents (I_{Total}; green). These outward currents are abolished by the application of the GABA receptor blockers gabazine and TPMPA (I_{Ca}; magenta). Inhibitory currents (I_{Inhib}; magenta) can be isolated by subtracting I_{Ca} (maroon) from I_{Total} (green). **(C)** Average whole-cell patch-clamp recordings from WT (blue; n = 6) and TPBG-KO (KO; orange; n = 5) RBCs to compare reciprocal inhibitory feedback ($I_{Inhib} = I_{Total} - I_{Ca}$) after a depolarizing pulse from -80 mV to -10 mV for 100 ms. The gray bar represents the region across which the charge transfer was calculated. **(D)** Quantification of the charge transfer (Q_{Inhib}) measured from baseline over the duration of the 100 ms stimulus. Ames medium was supplemented with 1 mM $CaCl_2$, 0.5 μM strychnine and 4 μM L-AP4. Open circles in bar graphs represent single cells and bars represent the mean ± SEM. Statistical significance was determined using Welch's t-tests; *: $p < 0.05$.

To test the hypothesis that reduced RBC glutamate release results in smaller inhibitory feedback currents in the TPBG-KO, we used whole-cell voltage-clamp to examine the reciprocal inhibitory response to a depolarizing pulse from -80 mV to -10 mV for 100 ms in WT (blue; n = 6) and TPBG-KO (KO; orange; n = 5) RBCs. L-AP4 was used to block spontaneous excitatory inputs and strychnine was used to block glycinergic inhibition. In the absence of GABA receptor blockers, outward currents can be seen superimposed on the evoked voltage-gated Ca^{2+} current (**Figure 7B; Green;** I_{Total}). Inhibitory currents (magenta; I_{Inhib}) can be isolated by subtracting voltage-gated Ca^{2+} currents (maroon; I_{Ca})from the total current. The charge transfer across the duration of the stimulus was reduced in the TPBG-KO compared to WT (**Figure 7D**; WT: 2.35 ± 0.37 pC; KO: 1.13 ± 0.22 pC; Welch's t-test: p = 0.022, t(7.83) = 2.83). This supports our previous result that the TPBG-KO suppresses RBC vesicle exocytosis and glutamate release (see **Figure 5F**).

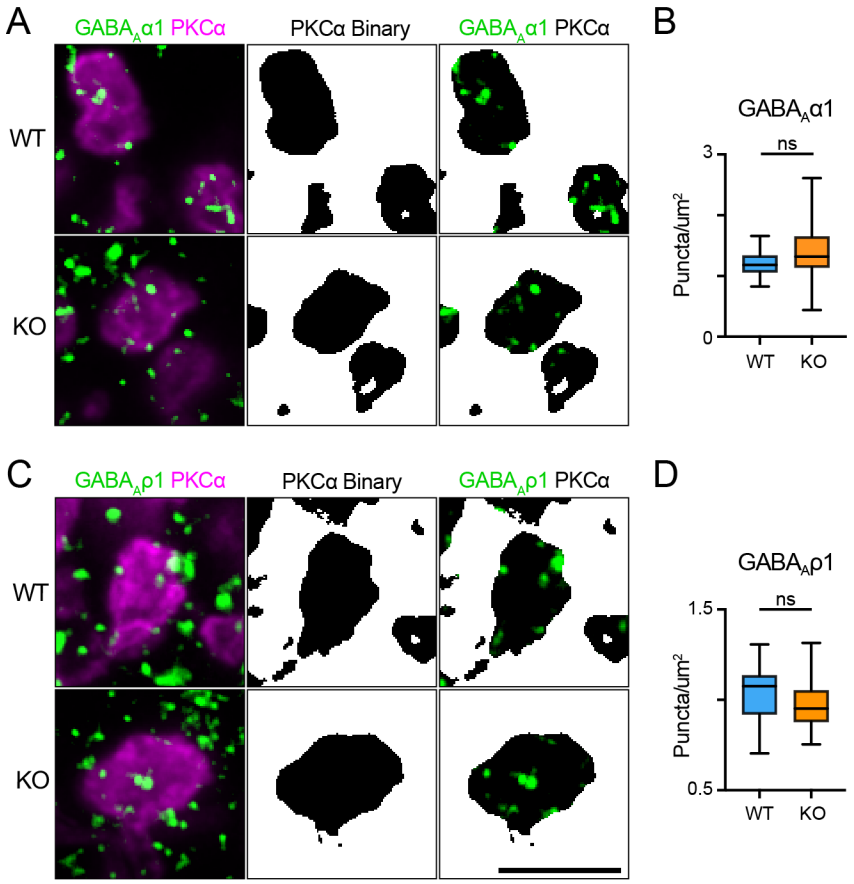

Figure 8: TPBG is not required for localization of GABA receptor immunofluorescence to RBC axon terminals. Immunofluorescence confocal microscopy of WT and TPBG-KO (KO) whole mount retinas using an antibody against PKCα (magenta) and antibodies against either the GABA$_A$α1 subunit (**A**; green; WT: *n* = 18 terminals; KO *n* = 28 terminals) or the GABA$_A$ρ1 subunit (**C**; green; WT: *n* = 20 terminals; KO *n* = 27 terminals). To isolate labeling in RBC axon terminals, binaries were created using the PKCα channel and overlayed over the other channels to generate binary masks. For all images, Z-projections of two sections were used with a Z-step distance of 0.297 μm for a total thickness of 0.547 μm. Scale bar is 5 μm. **(B)** Quantification of GABA$_A$α1 subunit puncta/μm^2. **(D)** Quantification of GABA$_A$α1 subunit puncta/μm^2. Box plots extend from the first to the third quartile and the whiskers extend across all points. The line in the box represents the median. Statistical significance was determined using Welch's *t*-tests; ns: $p > 0.05$.

It is possible that reciprocal feedback is altered in TPBG-KO due to disrupted expression or clustering of GABA receptors in RBC axon terminals. RBCs express both GABA$_A$α1 and GABA$_A$ρ1 receptor subunits in their axon terminals (Fletcher, Koulen, & Wässle, 1998; Palmer, 2006). To see whether TPBG-KO alters GABA receptor expression patterns, we used double immunofluorescence labeling of WT and TPBG-KO whole mount retinas using an antibody against PKCα and antibodies against GABA$_A$α1 (WT: *n* = 18 terminals from three animals; KO *n* = 28 terminals from four animals) and GABA$_A$ρ1 (WT: *n* = 20 terminals from three animals; KO *n* = 27 terminals from three animals) receptor subunits (**Figure 8**). As previously, we isolated RBC axon terminal-specific labeling using a binary mask derived from PKCα immunofluorescence.

644 Next, we counted the GABA puncta per unit area in PKCα-positive axon terminals. We did not
645 observe any major differences in puncta/μm^2 between WT and TPBG-KO (KO) retinas labeled
646 against either $GABA_A\alpha1$ (**Figure 8A-B**; WT: 1.21 $\pm$ 0.05 puncta/μm^2; KO: 1.40 $\pm$ 0.09 puncta/μm^2;
647 Welch's *t*-test: $p = 0.064$, $t(39.73) = 1.91$) or $GABA_A\rho1$ (**Figure 8C-D**; WT: 1.03 $\pm$ 0.03 puncta/μm^2;
648 KO: 0.98 $\pm$ 0.03 puncta/μm^2; Welch's *t*-test: $p = 0.20$, $t(41.11) = 1.29$), indicating that impaired
649 GABA receptor expression is likely not reducing inhibitory feedback. Taken together, our data
650 supports the conclusion that TPBG is required for normal synaptic ribbon development and
651 efficient glutamate release from RBC axon terminals.
652
653 **Discussion**
654 In this study, we characterized the functional consequences of genetic knockout of TPBG
655 in the mouse retina using immunofluorescence and electrophysiological approaches. TPBG-KO
656 did not alter gross RBC morphology in the OPL or IPL as PKCα-labeled RBC dendrites and axon
657 terminals appear normal in both conditions. Because TPBG is localized to both the dendrites and
658 axon terminals of RBCs (Wakeham et al., 2020), we sought to examine the effect of TPBG-KO
659 on the RBC synaptic structure and physiology in both compartments. Though ERG b-waves were
660 larger in the TPBG-KO, dendritic TRPM1 currents activated by CPPG did not change. In contrast
661 to the larger b-waves, the scotopic OPs were smaller in the KO, suggesting changes in RBC
662 ribbon synapse function. Accordingly, time-resolved C_m measurements and whole-cell recording
663 indicated that synaptic vesicle exocytosis and GABAergic feedback are reduced at TPBG-KO
664 RBC synapses, and synaptic ribbons are shorter. Importantly, we did not detect differences in
665 presynaptic voltage-gated Ca^{2+} current amplitude or changes in Ca^{2+} channel, GABA receptor, or
666 RIBEYE expression and localization. We propose that TPBG plays an important role in fine tuning
667 the synaptic architecture of RBC ribbon synapses to increase exocytosis efficiency.
668
669 *TPBG and RBC dendrites*
670 We found that TPBG is not required for the normal insertion of RBC dendritic tips inside
671 rod spherules or for normal depolarizing currents through TRPM1 cation channels. Our
672 immunofluorescence and electrophysiological examination of RBC dendrites suggest that TPBG
673 is not essential for basic synaptic function in that compartment. That being said, TPBG
674 immunofluorescence reveals that large amounts of TPBG are present in RBC dendrites,
675 suggesting some role in dendritic development or physiology.
676 TPBG regulates dendritic arborization in mouse olfactory bulb granule cells (Yoshihara et
677 al., 2012). In these neurons, TPBG-KO reduced dendritic branching and dendritic migration to

678 synaptic targets. Lentiviral overexpression of TPBG increased dendritic branching complexity and
679 restored dendritic arborization deficits induced by nasal occlusion. In the retina, TPBG may also
680 regulate RBC dendritic branching complexity in the OPL. TPBG is a known regulator of Wnt
681 signaling (He et al., 2015; Kagermeier-Schenk et al., 2011), which is required for functional
682 synaptic targeting and OPL lamination in RBCs, therefore TPBG may promote RBC dendritic
683 development through control of the Wnt pathway (Tsuboi, 2020). We didn't detect a structural or
684 physiological phenotype in RBC dendrites, but thorough evaluation of RBC dendritic maturation
685 and branching using sparse labeling techniques might reveal a more subtle effect of TPBG-KO
686 on dendritic architecture.
687
688 *TPBG and RBC synaptic vesicle exocytosis*
689 We found a reduction in the OPs isolated from scotopic ERG recordings in TPBG-KO
690 mice, which we interpret as evidence for decreased RBC output to third-order neurons. While we
691 cannot rule out a contribution of the TPBG-expressing amacrine cells to the reduced OP
692 amplitudes in the TPBG-KO, the similarity of the OP phenotype to that seen in the PKCα-KO
693 (Xiong et al., 2015) suggests that it is due to an RBC defect. Furthermore, pharmacological
694 dissection of ERG components points to the RBC to AII/A17 reciprocal synapse as the origin of
695 the OPs (Liao, Liu, Milla-Navarro, Villa, & Germain, 2023; Wachtmeister, 1998). Early studies
696 implicated interactions between bipolar cell axon terminals, amacrine cell processes, and
697 ganglion cell dendrites as potential generators of the OPs (Ogden, 1973). Intravitreal injections of
698 glycine into rabbit retinas resulted in morphological changes in many ACs and disappearance of
699 the OPs from the ERG (Korol, Leuenberger, Englert, & Babel, 1975) while application of
700 neurotoxic kainate to ganglion cell dendrites diminishes OP amplitude (Vaegan & Millar, 1994). A
701 more recent study unequivocally implicates multiple distinct generators in the production of early,
702 intermediate, and late OP peaks (Dong, Agey, & Hare, 2004). The use of APB and CNQX to block
703 synaptic inputs to ON and OFF-bipolar cells significantly diminished intermediate and later OPs
704 but left early OPs intact, suggesting that early OPs are generated by photoreceptors. Intermediate
705 and late OPs have differential sensitivity to tetrodotoxin, which abolished only late OPs, indicating
706 that intermediate OPs are generated by action-potential-independent interactions and late OPs
707 are generated by action-potential-dependent ones (Dong et al., 2004). Our OP data shows a
708 much larger attenuation of TPBG-KO OP amplitude in intermediate and late OPs compared to
709 early ones. Thus, the results of these studies support our conclusion that reduced scotopic OPs
710 are likely due to suppressed rhythmic activity of third-order neurons due to reduced RBC
711 glutamate release.

712 By simultaneously recording the presynaptic voltage-gated Ca^{2+} currents and subsequent
713 membrane capacitance changes evoked by RBC depolarization, we showed that reduced
714 exocytosis in TPBG-KO RBCs compared to WT, despite no change in presynaptic Ca^{2+} currents,
715 indicating reduced exocytosis efficiency in the TPBG-KO. The Ca^{2+} current amplitudes we
716 recorded (-75 pA) following a depolarizing step are significantly larger than those previously
717 reported (-30 pA by (Protti & Llano, 1998) and -20 pA by (Singer & Diamond, 2003)). We also
718 recorded larger C_m jumps (42 fF in WT) than those reported from dissociated RBCs (30 fF in
719 (Zhou, Wan, Thakur, & Heidelberger, 2006)). We believe these differences can be attributed to
720 higher recording temperatures (33° C vs 21° C) and our use of older animals. With a mean resting
721 C_m of 5.97 pF and a mean R_s of 50.04 MΩ, we can calculate an average voltage-clamp speed of
722 298.74 μs – sufficiently fast to clamp the membrane to a 200 Hz sine wave with a 5 ms period.
723 The reduced exocytosis in the TPBG-KO, despite the same Ca^{2+} currents as in WT, suggests that
724 calcium influx is not as tightly coupled to the synaptic vesicle exocytosis in the TPBG-KO, resulting
725 in reduced exocytosis efficiency.
726 Exocytosis efficiency is calculated as the exocytosis per unit Ca^{2+} charge transfer. We
727 calculated an exocytosis efficiency of approximately 6 fF/pC in adult WT mouse RBCs after a 100
728 ms depolarizing pulse at 33° C. In adult vertebrate auditory hair cells, which also form ribbon
729 synapses, similar exocytosis efficiencies of 5 to 6 fF/pC have been reported after 100 ms pulses
730 (Chen & von Gersdorff, 2019; Moser et al., 2020). Rod bipolar cell ribbon synapses operate via
731 nanodomain coupling between Ca^{2+} channels and docked vesicles (Jarsky et al., 2010), whereas
732 immature calyx of Held synapses contain conventional active zones that operate via Ca^{2+}
733 microdomains where Ca^{2+} influx triggers vesicle exocytosis from greater distances (Kushmerick,
734 Renden, & von Gersdorff, 2006). Nevertheless, exocytosis efficiency can still be as high as 16 to
735 20 fF/pC at immature calyx of Held axon terminals after a short 1 ms pulse. Further studies will
736 be required to verify the relationship between TPBG and nanodomain coupling at RBC ribbon
737 synapses.
738
739 *TPBG and synaptic ribbon proteins*
740 Neurotransmitter release from synaptic ribbons can be simplified into three major steps:
741 synaptic docking, Ca^{2+} influx and its detection by Ca^{2+} sensors, and Ca^{2+}-dependent fusion of
742 synaptic vesicles with the presynaptic membrane (Dieck & Brandstätter, 2006; Morgans, 2000).
743 These are all potential points at which TPBG may be supporting efficient vesicle release from
744 RBCs. Vesicle accumulation and transport in RBC synaptic terminals is dependent on F-actin
745 polymerization and is regulated by PKCα (Berglund, Midorikawa, & Tachibana, 2002; Doussau &

746 Augustine, 2000; Job & Lagnado, 1998; Minami, Berglund, Sakaba, Kohmoto, & Tachibana, 1998;
747 Tachibana, 1999). We originally identified TPBG as a PKCα-dependent phosphoprotein
748 (Wakeham et al., 2019); thus, it is possible that PKCα controls vesicle docking via actin dynamics
749 in RBC axon terminals through TPBG.

750 The tight temporal control of vesicle release that is a trademark of synaptic ribbons
751 requires nanodomain-coupling between L-type voltage-gated Ca^{2+} channels and Ca^{2+} binding
752 proteins that trigger synaptic vesicle fusion (Balakrishnan et al., 2015; Eggermann, Bucurenciu,
753 Goswami, & Jonas, 2012; Jarsky et al., 2010). Synaptic ribbons are primarily composed of the
754 scaffold protein RIBEYE and are anchored to the presynaptic active zone by a number of
755 cytoskeletal anchoring proteins, including Bassoon and Piccolo (Zanazzi & Matthews, 2009). We
756 did not observe a difference in RIBEYE immunofluorescence in WT and TPBG-KO axon
757 terminals, but immunofluorescence does not have the resolution to confirm the correct localization
758 or orientation of the ribbon at the active zone, If TPBG is required for correct localization of the
759 ribbon, exocytosis efficiency may be significantly disrupted in KO RBCs, but electron microscopy
760 showed normal positioning of ribbons at RBC active zones in the KO. $Ca_v1.4$ and RIBEYE appear
761 co-localized by immunofluorescence in both WT and TPBG-KO RBC axon terminals, but a small
762 disruption of this tight coupling might not be detected with immunofluorescence and could have a
763 large effect on glutamate release by slowing the accumulation of Ca^{2+} at the sensor. Nanodomain
764 coupling likely depends on a close spatial relationship between the L-type channels and the
765 vesicle release machinery, yet it is not fully known how this clustering is achieved in RBCs. It is
766 possible that TPBG facilitates Ca^{2+} channel clustering or association between the channels and
767 the ribbon such that, in its absence, normal nanodomain coupling is disrupted and synaptic vesicle
768 fusion is reduced.

769 Ultrastructural analysis of RBC axon terminals revealed that the synaptic ribbons are
770 approximately 15% smaller in TPBG-KO RBCs compared to WT. Shorter ribbons could result in
771 a smaller number of ribbon-attached vesicles that may constitute a smaller ready releasable pool
772 (RRP), resulting in the observed C_m jump attenuation. The density of ribbons was not reduced in
773 the TPBG-KO as assayed by immunofluorescence imaging, nor were Ca^{2+} currents changed;
774 thus, the smaller C_m jumps not could be due to a smaller number of ribbons or reduced Ca^{2+} influx.
775 We used a large 100 ms depolarizing pulse to evoke vesicle release which likely exhausts the
776 fast RRP (docked vesicles) and potentially depletes the secondary RRP (vesicles attached to the
777 ribbon in upper rows). The fast RRP probably consists of the first row of vesicles lining the bottom
778 of the ribbon closest to the active zone (von Gersdorff & Matthews, 1997; von Gersdorff et al.,
779 1996) and this pool may not be affected by a shorter ribbon. In contrast, a shorter ribbon may

780 significantly reduce the size of the secondary RRP, presumably corresponding to vesicles
781 tethered higher on the ribbon, leading to reduced C_m jumps. Indeed, in RIBEYE-KO mice, where
782 the synaptic ribbon is absent, exocytosis is greatly reduced in RBC and rod photoreceptor
783 synapses (Grabner & Moser, 2021; Maxeiner, Luo, Tan, Schmitz, & Südhof, 2016). More
784 experimentation is required to determine exactly how the shorter ribbons in the TPBG-KO RBC
785 axon terminals affects the different vesicle pools.
786
787 *TPBG and reciprocal feedback inhibition*
788 To confirm that the TPBG-KO reduces RBC vesicle fusion and glutamate release, we
789 compared GABAergic feedback inhibition between WT and TPBG-KO RBCs. We found
790 attenuation of inhibitory charge transfer in the TPBG-KO. With glycinergic inhibition blocked by
791 strychnine, the primary remaining source of feedback inhibition in RBCs is A17-mediated
792 GABAergic reciprocal feedback. GABA released from A17-ACs is sensed by two kinetically
793 distinct ionotropic GABA receptors in RBC axon terminals: $GABA_A$ and $GABA_A\rho$ (Fletcher et al.,
794 1998). $GABA_A$ receptor-mediated current is rapidly-activating, while $GABA_A\rho$-mediated current is
795 slowly-activating (Grimes et al., 2015). We detected two different inhibitory components: a large,
796 quickly-inactivating current and a smaller sustained one. Though we did not pharmacologically
797 isolate each current, the kinetics of the inhibitory currents suggest that peak I_{Inhib} is likely mediated
798 by $GABA_A$ receptors and sustained I_{Inhib} is likely mediated by $GABA_A\rho$ receptors. We note that our
799 peak WT $GABA_A$ receptor currents of ~125 pA and sustained $GABA_A\rho$ receptor currents of ~50
800 pA are considerably larger than reported previously in mouse RBCs (Chávez et al., 2010). Again,
801 we attribute this to our use of older animals and higher recording temperatures and, perhaps, the
802 use of Ames recording solutions: Ames contains ascorbic acid, which is an enhancer of GABA
803 currents (Calero et al., 2011).
804 GABAergic reciprocal feedback from A17-ACs might be altered if GABA receptor
805 expression or localization was disrupted by TPBG-KO. $GABA_A$ receptors are large pentameric ion
806 channels usually containing α, β, and γ subunits. Early work indicates that RBC axon terminals
807 express $GABA_A\alpha1$, $\alpha3$, and $\gamma2$ receptor subunits (Fletcher et al., 1998), but a recent study found
808 that the $\alpha1$ subunit dominates in adult mice (Sinha et al., 2021). $GABA_A\rho$ receptors contain only
809 ρ subunits (Fletcher et al., 1998). Therefore, we used antibodies against $GABA_A\alpha1$ and $GABA_A\rho1$
810 to visualize $GABA_A$ and $GABA_A\rho$ receptor localization and an antibody against PKCα to isolate
811 RBC-specific axon terminals. We did not detect any difference in GABA receptor

812 immunofluorescence in RBC axon terminals between WT and TPBG-KO, indicating that reduced
813 GABAergic feedback is likely not due to disrupted GABA receptor localization.
814 We found that TPBG-KO increased scotopic ERG b-waves, suggesting an increase in
815 RBC depolarization. The scotopic ERG b-wave is initiated by current through TRPM1 non-specific
816 cation channels in the RBC dendrites. Yet, we did not find any difference in CPPG-induced
817 TRPM1 currents between WT and TPBG-KO retinas and the input resistance and excitability of
818 the RBC was unchanged. However, the scotopic b-wave is also shaped by reciprocal inhibition.
819 Pharmacological studies show that blocking inhibitory currents from third-order neurons changes
820 the scotopic b-wave. In particular, injections of a $GABA_A$ antagonist (bicuculline) or a $GABA_{A\rho}$
821 antagonist (TPMPA) into the IPL significantly increases the amplitude and duration of the scotopic
822 b-wave (Dong & Hare, 2000, 2003), suggesting that GABAergic feedback from A17-ACs
823 contributes to the shape of the RBC light response. We suggest that the enlarged ERG b-wave
824 in the TPBG-KO is due to reduced inhibitory feedback onto the RBC terminals, secondary to
825 reduced RBC glutamate release by the RBC.
826
827 *Summary*
828 Our findings show that genetic deletion of TPBG attenuates scotopic ERG oscillatory
829 potentials, synaptic vesicle exocytosis from RBCs, and reciprocal feedback onto RBCs. We
830 propose that TPBG is required for efficient coupling of Ca^{2+} influx and glutamate release at RBC
831 active zones, possibly through its effect on synaptic ribbons. Further evaluation of TPBG is critical
832 for producing a more comprehensive understanding of its role in fine-tuning RBC synaptic ribbon
833 physiology.

834 **Figure Supplements**
835

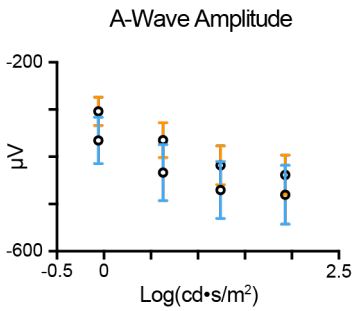

836
837 ***Figure 2 Supplementary Figure: TPBG-KO does not alter the scotopic ERG a-wave***. Quantification of a-wave
838 amplitudes recorded after light stimuli (-0.06 to 1.93 log(cd•s/m^2)). A-waves are measured from baseline to the a-wave
839 trough. Data is presented as the mean ± SEM.
840

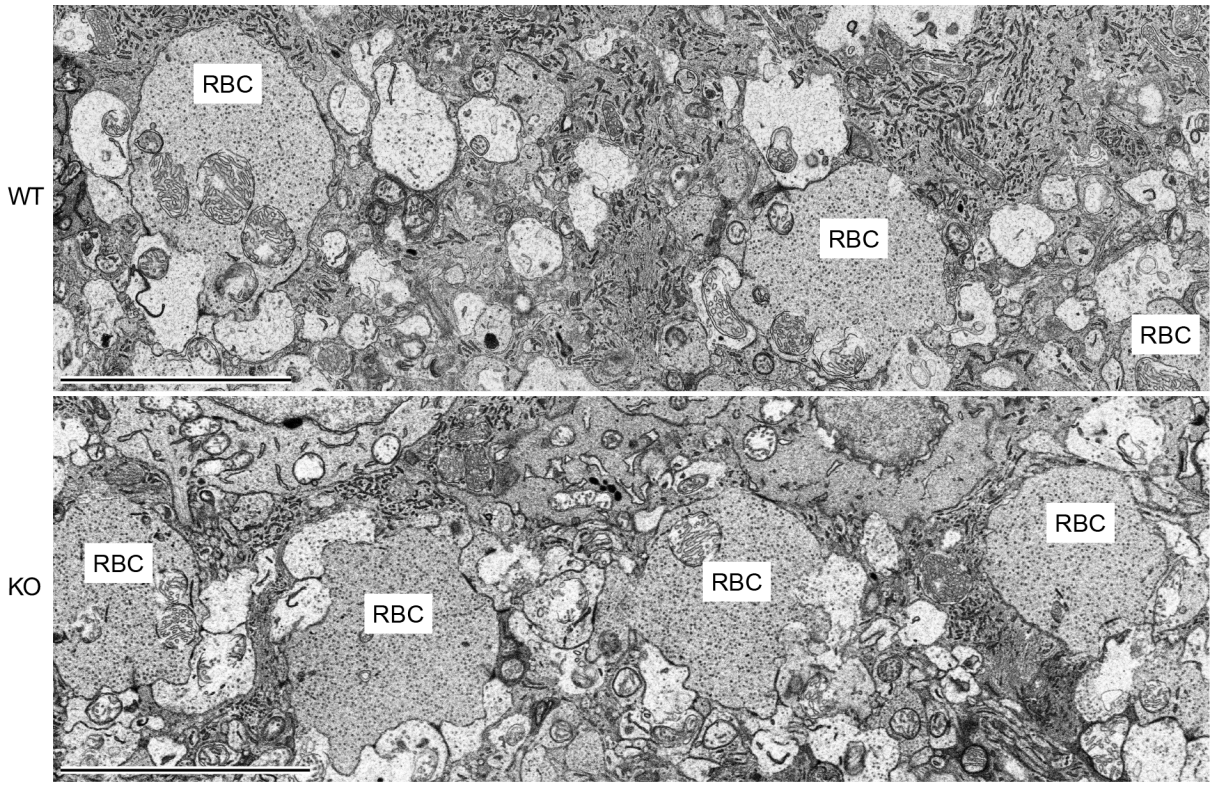

Figure 4 Supplementary Figure: FIB-SEM imaging of RBC axon terminals. Focused ion beam scanning electron microscopy (FIB-SEM) was used to image RBC axon terminals in the distal IPL and examine synaptic ribbon location and morphology. Zoomed-out examples of WT and TPBG-KO (KO) RBC axon terminals in the IPL. The scale bar is 5 μm.

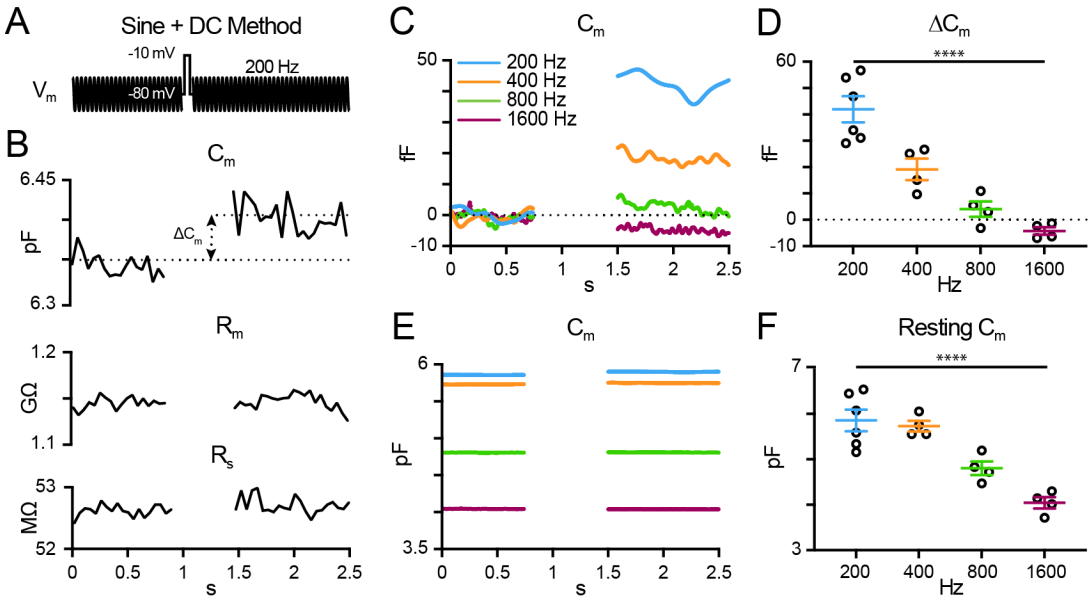

Figure 5 Supplementary Figure: Measuring membrane capacitance in RBCs. **(A)** Whole-cell voltage-clamp capacitance recordings were made using the "sine + DC" method. A sinusoidal voltage command (200 Hz at 30 mV trough-to-peak) was superimposed on the holding potential of -80 mV. Membrane capacitance (C_m), membrane resistance (R_m), and series resistance (R_s) were recorded before and after a depolarizing pulse from -80 mV to -10 mV for 100 ms. **(B)** A sample recording from a WT RBC using the sine + DC method as described. The change in membrane capacitance (ΔC_m) was measured as the difference between the C_m before and after the depolarizing pulse. Changes to R_m (middle) and R_s (bottom) were small and do not correlate with changes in C_m. **(C)** Average baseline-subtracted C_m recordings using 200 Hz (blue; n = 6), 400 Hz (orange; n = 4), 800 Hz (green; n = 4), or 1600 Hz (magenta; n = 4) sinusoidal voltage commands in WT RBCs. Data for the 200 Hz condition was reused from WT in Figure 4. Traces with higher frequencies were resampled to 200 Hz for ease of comparisons. **(D)** Quantification of ΔC_m. **(E)** Average C_m recordings and **(F)** quantification of resting C_m across frequencies. Resting C_m was measured before the depolarizing pulse. Open circles in bar graphs represent single cells and bars represent the mean ± SEM. Statistical significance was determined using Brown-Forsythe ANOVA tests; ****: $p < 0.0001$.

References

Agosto, M. A., & Wensel, T. G. (2020). LRRTM4 is a member of the transsynaptic complex between rod photoreceptors and bipolar cells. *Journal of Comparative Neurology*, *529*(1), 221–233. doi: 10.1002/cne.24944

Balakrishnan, V., Puthussery, T., Kim, M.-H., Taylor, W. R., & von Gersdorff, H. (2015). Synaptic Vesicle Exocytosis at the Dendritic Lobules of an Inhibitory Interneuron in the Mammalian Retina. *Neuron*, *87*(3), 563–575. doi: 10.1016/j.neuron.2015.07.016

Berglund, K., Midorikawa, M., & Tachibana, M. (2002). Increase in the Pool Size of Releasable Synaptic Vesicles by the Activation of Protein Kinase C in Goldfish Retinal Bipolar Cells. *The Journal of Neuroscience*, *22*(12), 4776–4785. doi: 10.1523/jneurosci.22-12-04776.2002

Calero, C. I., Vickers, E., Cid, G. M., Aguayo, L. G., von Gersdorff, H., & Calvo, D. J. (2011). Allosteric modulation of retinal GABA receptors by ascorbic acid. *The Journal of Neuroscience : The Official Journal of the Society for Neuroscience*, *31*(26), 9672–9682. doi: 10.1523/jneurosci.5157-10.2011

Cao, Y., Posokhova, E., & Martemyanov, K. A. (2011). TRPM1 Forms Complexes with Nyctalopin In Vivo and Accumulates in Postsynaptic Compartment of ON-Bipolar Neurons in mGluR6-Dependent Manner. *The Journal of Neuroscience*, *31*(32), 11521–11526. doi: 10.1523/jneurosci.1682-11.2011

Cao, Y., Sarria, I., Fehlhaber, K. E., Kamasawa, N., Orlandi, C., James, K. N., … Martemyanov, K. A. (2015). Mechanism for Selective Synaptic Wiring of Rod Photoreceptors into the Retinal Circuitry and Its Role in Vision. *Neuron*, *87*(6), 1248–1260. doi: 10.1016/j.neuron.2015.09.002

Cao, Y., Wang, Y., Dunn, H. A., Orlandi, C., Shultz, N., Kamasawa, N., … Martemyanov, K. A. (2020). Interplay between cell-adhesion molecules governs synaptic wiring of cone photoreceptors. *Proceedings of the National Academy of Sciences*, *117*(38), 23914–23924. doi: 10.1073/pnas.2009940117

Chávez, A. E., Grimes, W. N., & Diamond, J. S. (2010). Mechanisms Underlying Lateral GABAergic Feedback onto Rod Bipolar Cells in Rat Retina. *The Journal of Neuroscience*, *30*(6), 2330–2339. doi: 10.1523/jneurosci.5574-09.2010

Chávez, A. E., Singer, J. H., & Diamond, J. S. (2006). Fast neurotransmitter release triggered by Ca influx through AMPA-type glutamate receptors. *Nature*, *443*(7112), 705–708. doi: 10.1038/nature05123

Chen, M., & von Gersdorff, H. (2019). How to Build a Fast and Highly Sensitive Sound Detector That Remains Robust to Temperature Shifts. *The Journal of Neuroscience*, *39*(37), 7260–7276. doi: 10.1523/jneurosci.2510-18.2019

Dieck, S. T., & Brandstätter, J. H. (2006). Ribbon synapses of the retina. *Cell and Tissue Research*, *326*(2), 339–346. doi: 10.1007/s00441-006-0234-0

Dong, C.-J., Agey, P., & Hare, W. A. (2004). Origins of the electroretinogram oscillatory potentials in the rabbit retina. *Visual Neuroscience*, *21*(4), 533–543. doi: 10.1017/s0952523804214043

Dong, C.-J., & Hare, W. A. (2000). Contribution to the kinetics and amplitude of the electroretinogram b-wave by third-order retinal neurons in the rabbit retina. *Vision Research*, *40*(6), 579–590. doi: 10.1016/s0042-6989(99)00203-5

Dong, C.-J., & Hare, W. A. (2003). Temporal Modulation of Scotopic Visual Signals by A17 Amacrine Cells in Mammalian Retina In Vivo. *Journal of Neurophysiology*, *89*(4), 2159–2166. doi: 10.1152/jn.01008.2002

Doussau, F., & Augustine, G. J. (2000). The actin cytoskeleton and neurotransmitter release: An overview. *Biochimie*, *82*(4), 353–363. doi: 10.1016/s0300-9084(00)00217-0

Eggermann, E., Bucurenciu, I., Goswami, S. P., & Jonas, P. (2012). Nanodomain coupling between Ca2+ channels and sensors of exocytosis at fast mammalian synapses. *Nature Reviews Neuroscience*, *13*(1), 7–21. doi: 10.1038/nrn3125

Euler, T., & Masland, R. H. (2000). Light-Evoked Responses of Bipolar Cells in a Mammalian Retina. *Journal of Neurophysiology*, *83*(4), 1817–1829. doi: 10.1152/jn.2000.83.4.1817

Famiglietti, E. V., & Kolb, H. (1975). A bistratified amacrine cell and synaptic cirucitry in the inner plexiform layer of the retina. *Brain Research*, *84*(2), 293–300.

Fletcher, E. L., Koulen, P., & Wässle, H. (1998). GABAA and GABAC receptors on mammalian rod bipolar cells. *Journal of Comparative Neurology*, *396*(3), 351–365. doi: 10.1002/(sici)1096-9861(19980706)396:3<351::aid-cne6>3.0.co;2-1

Gillis, K. D. (2000). Admittance-based measurement of membrane capacitance using the EPC-9 patch-clamp amplifier. *Pflügers Archiv*, *439*(5), 655–664. doi: 10.1007/s004249900173

Grabner, C. P., & Moser, T. (2021). The mammalian rod synaptic ribbon is essential for Cav channel facilitation and ultrafast synaptic vesicle fusion. *ELife*, *10*, e63844. doi: 10.7554/elife.63844

Grimes, W. N., Zhang, J., Graydon, C. W., Kachar, B., & Diamond, J. S. (2010). Retinal Parallel Processors: More than 100 Independent Microcircuits Operate within a Single Interneuron. *Neuron*, *65*(6), 873–885. doi: 10.1016/j.neuron.2010.02.028

Grimes, W. N., Zhang, J., Tian, H., Graydon, C. W., Hoon, M., Rieke, F., & Diamond, J. S. (2015). Complex inhibitory microcircuitry regulates retinal signaling near visual threshold. *Journal of Neurophysiology*, *114*(1), 341–353. doi: 10.1152/jn.00017.2015

Hartveit, E. (1996). Membrane currents evoked by ionotropic glutamate receptor agonists in rod bipolar cells in the rat retinal slice preparation. *Journal of Neurophysiology*, *76*(1), 401–422. doi: 10.1152/jn.1996.76.1.401

Hartveit, E. (1999). Reciprocal Synaptic Interactions Between Rod Bipolar Cells and Amacrine Cells in the Rat Retina. *Journal of Neurophysiology*, *81*(6), 2923–2936. doi: 10.1152/jn.1999.81.6.2923

Hasan, N., Pangeni, G., Cobb, C. A., Ray, T. A., Nettesheim, E. R., Ertel, K. J., … Gregg, R. G. (2019). Presynaptic Expression of LRIT3 Transsynaptically Organizes the Postsynaptic Glutamate Signaling Complex Containing TRPM1. *Cell Reports*, *27*(11), 3107-3116.e3. doi: 10.1016/j.celrep.2019.05.056

Hasan, N., Pangeni, G., Ray, T. A., Fransen, K. M., Noel, J., Borghuis, B. G., … Gregg, R. G. (2020). LRIT3 is required for Nyctalopin expression and normal ON and OFF pathway signaling in the retina. *ENeuro*, *7*(1), ENEURO.0002-20.2020. doi: 10.1523/eneuro.0002-20.2020

Hasan, N., Ray, T. A., & Gregg, R. G. (2016). CACNA1S expression in mouse retina: Novel isoforms and antibody cross-reactivity with GPR179. *Visual Neuroscience*, *33*, E009. doi: 10.1017/s0952523816000055

He, P., Jiang, S., Ma, M., Wang, Y., Li, R., Fang, F., … Zhang, Z. (2015). Trophoblast glycoprotein promotes pancreatic ductal adenocarcinoma cell metastasis through Wnt/planar cell polarity signaling. *Molecular Medicine Reports*, *12*(1), 503–509. doi: 10.3892/mmr.2015.3412

Jarsky, T., Tian, M., & Singer, J. H. (2010). Nanodomain Control of Exocytosis Is Responsible for the Signaling Capability of a Retinal Ribbon Synapse. *Journal of Neuroscience*, *30*(36), 11885–11895. doi: 10.1523/jneurosci.1415-10.2010

Job, C., & Lagnado, L. (1998). Calcium and Protein Kinase C Regulate the Actin Cytoskeleton in the Synaptic Terminal of Retinal Bipolar Cells. *The Journal of Cell Biology*, *143*(6), 1661–1672. doi: 10.1083/jcb.143.6.1661

Kagermeier-Schenk, B., Wehner, D., Özhan-Kizil, G., Yamamoto, H., Li, J., Kirchner, K., … Weidinger, G. (2011). Waif1/5T4 Inhibits Wnt/β-Catenin Signaling and Activates Noncanonical Wnt Pathways by Modifying LRP6 Subcellular Localization. *Developmental Cell*, *21*(6), 1129–1143. doi: 10.1016/j.devcel.2011.10.015

Kim, M.-H., & von Gersdorff, H. (2016). Postsynaptic Plasticity Triggered by Ca^{2+}-Permeable AMPA Receptor Activation in Retinal Amacrine Cells. *Neuron*, *89*(3), 507–520. doi: 10.1016/j.neuron.2015.12.028

Klyachko, V. A., & Jackson, M. B. (2002). Capacitance steps and fusion pores of small and large-dense-core vesicles in nerve terminals. *Nature*, *418*(6893), 89–92. doi: 10.1038/nature00852

Kobe, B., & Deisenhofer, J. (1994). The leucine-rich repeat: a versatile binding motif. *Trends in Biochemical Sciences*, *19*(10), 415–421. doi: 10.1016/0968-0004(94)90090-6

Kobe, B., & Kajava, A. V. (2001). The leucine-rich repeat as a protein recognition motif. *Current Opinion in Structural Biology*, *11*(6), 725–732. doi: 10.1016/s0959-440x(01)00266-4

Koike, C., Numata, T., Ueda, H., Mori, Y., & Furukawa, T. (2010). TRPM1: A vertebrate TRP channel responsible for retinal ON bipolar function. *Cell Calcium*, *48*(2–3), 95–101. doi: 10.1016/j.ceca.2010.08.004

Koike, C., Obara, T., Uriu, Y., Numata, T., Sanuki, R., Miyata, K., … Furukawa, T. (2010). TRPM1 is a component of the retinal ON bipolar cell transduction channel in the mGluR6 cascade. *Proceedings of the National Academy of Sciences*, *107*(1), 332–337. doi: 10.1073/pnas.0912730107

Korol, S., Leuenberger, P. M., Englert, U., & Babel, J. (1975). In vivo effects of glycine on retinal ultrastructure and averaged electroretinogram. *Brain Research*, *97*(2), 235–251. doi: 10.1016/0006-8993(75)90447-3

Kushmerick, C., Renden, R., & von Gersdorff, H. (2006). Physiological Temperatures Reduce the Rate of Vesicle Pool Depletion and Short-Term Depression via an Acceleration of Vesicle Recruitment. *The Journal of Neuroscience*, *26*(5), 1366–1377. doi: 10.1523/jneurosci.3889-05.2006

Liao, F., Liu, H., Milla-Navarro, S., Villa, P. de la, & Germain, F. (2023). Origin of Retinal Oscillatory Potentials in the Mouse, a Tool to Specifically Locate Retinal Damage. *International Journal of Molecular Sciences*, *24*(4), 3126. doi: 10.3390/ijms24043126

Masu, M., Iwakabe, H., Tagawa, Y., Miyoshi, T., Yamashita, M., Fukuda, Y., … Nakanishi, S. (1995). Specific deficit of the ON response in visual transmission by targeted disruption of the mGIuR6 gene. *Cell*, *80*(5), 757–765. doi: 10.1016/0092-8674(95)90354-2

Maxeiner, S., Luo, F., Tan, A., Schmitz, F., & Südhof, T. C. (2016). How to make a synaptic ribbon: RIBEYE deletion abolishes ribbons in retinal synapses and disrupts neurotransmitter release. *The EMBO Journal*, *35*(10), 1098–1114. doi: 10.15252/embj.201592701

McGuire, B., Stevens, J., & Sterling, P. (1984). Microcircuitry of bipolar cells in cat retina. *The Journal of Neuroscience*, *4*(12), 2920–2938. doi: 10.1523/jneurosci.04-12-02920.1984

Minami, N., Berglund, K., Sakaba, T., Kohmoto, H., & Tachibana, M. (1998). Potentiation of transmitter release by protein kinase C in goldfish retinal bipolar cells. *The Journal of Physiology*, *512*(1), 219–225. doi: 10.1111/j.1469-7793.1998.219bf.x

Morgans, C. W. (2000). Neurotransmitter release at ribbon synapses in the retina. *Immunology and Cell Biology*, *78*(4), 442–446. doi: 10.1046/j.1440-1711.2000.00923.x

Morgans, C. W., Zhang, J., Jeffrey, B. G., Nelson, S. M., Burke, N. S., Duvoisin, R. M., & Brown, R. L. (2009). TRPM1 is required for the depolarizing light response in retinal ON-bipolar cells. *Proceedings of the National Academy of Sciences*, *106*(45), 19174–19178. doi: 10.1073/pnas.0908711106

Moser, T., Grabner, C. P., & Schmitz, F. (2020). Sensory Processing at Ribbon Synapses in the Retina and the Cochlea. *Physiological Reviews*, *100*(1), 103–144. doi: 10.1152/physrev.00026.2018

1009 Nakajima, Y., Iwakabe, H., Akazawa, C., Nawa, H., Shigemoto, R., Mizuno, N., & Nakanishi, S.
1010 (1993). Molecular characterization of a novel retinal metabotropic glutamate receptor
1011 mGluR6 with a high agonist selectivity for L-2-amino-4-phosphonobutyrate. *The Journal of*
1012 *Biological Chemistry*, *268*(16), 11868–11873.

1013 Neher, E., & Marty, A. (1982). Discrete changes of cell membrane capacitance observed under
1014 conditions of enhanced secretion in bovine adrenal chromaffin cells. *Proceedings of the*
1015 *National Academy of Sciences*, *79*(21), 6712–6716. doi: 10.1073/pnas.79.21.6712

1016 Neuillé, M., Cao, Y., Caplette, R., Guerrero-Given, D., Thomas, C., Kamasawa, N., … Zeitz, C.
1017 (2017). LRIT3 Differentially Affects Connectivity and Synaptic Transmission of Cones to ON-
1018 and OFF-Bipolar CellsLRIT3's Role in Cone to Bipolar Cell Transmission. *Investigative*
1019 *Ophthalmology & Visual Science*, *58*(3), 1768–1778. doi: 10.1167/iovs.16-20745

1020 Neuillé, M., Morgans, C. W., Cao, Y., Orhan, E., Michiels, C., Sahel, J., … Zeitz, C. (2015).
1021 LRIT3 is essential to localize TRPM1 to the dendritic tips of depolarizing bipolar cells and
1022 may play a role in cone synapse formation. *European Journal of Neuroscience*, *42*(3), 1966–
1023 1975. doi: 10.1111/ejn.12959

1024 Ogden, T. E. (1973). The oscillatory waves of the primate electroretinogram. *Vision Research*,
1025 *13*(6), 1059-IN4. doi: 10.1016/0042-6989(73)90144-2

1026 Oltedal, L., & Hartveit, E. (2010). Transient release kinetics of rod bipolar cells revealed by
1027 capacitance measurement of exocytosis from axon terminals in rat retinal slices. *The Journal*
1028 *of Physiology*, *588*(9), 1469–1487. doi: 10.1113/jphysiol.2010.186916

1029 Oltedal, L., Veruki, M. L., & Hartveit, E. (2009). Passive membrane properties and electrotonic
1030 signal processing in retinal rod bipolar cells. *The Journal of Physiology*, *587*(4), 829–849.
1031 doi: 10.1113/jphysiol.2008.165415

1032 Palmer, M. J. (2006). Functional segregation of synaptic GABAA and GABAC receptors in
1033 goldfish bipolar cell terminals. *The Journal of Physiology*, *577*(1), 45–53. doi:
1034 10.1113/jphysiol.2006.119560

1035 Paridaen, J. T. M. L., Wilsch-Bräuninger, M., & Huttner, W. B. (2013). Asymmetric Inheritance of
1036 Centrosome-Associated Primary Cilium Membrane Directs Ciliogenesis after Cell Division.
1037 *Cell*, *155*(2), 333–344. doi: 10.1016/j.cell.2013.08.060

1038 Pearring, J. N., Bojang, P., Shen, Y., Koike, C., Furukawa, T., Nawy, S., & Gregg, R. G. (2011).
1039 A Role for Nyctalopin, a Small Leucine-Rich Repeat Protein, in Localizing the TRP
1040 Melastatin 1 Channel to Retinal Depolarizing Bipolar Cell Dendrites. *The Journal of*
1041 *Neuroscience*, *31*(27), 10060–10066. doi: 10.1523/jneurosci.1014-11.2011

1042 Protti, D. A., & Llano, I. (1998). Calcium Currents and Calcium Signaling in Rod Bipolar Cells of
1043 Rat Retinal Slices. *Journal of Neuroscience*, *18*(10), 3715–3724. doi: 10.1523/jneurosci.18-
1044 10-03715.1998

1045 Raviola, E., & Dacheux, R. F. (1987). Excitatory dyad synapse in rabbit retina. *Proceedings of*
1046 *the National Academy of Sciences*, *84*(20), 7324–7328. doi: 10.1073/pnas.84.20.7324

Robson, J. G., & Frishman, L. J. (2014). The rod-driven a-wave of the dark-adapted mammalian electroretinogram. *Progress in Retinal and Eye Research*, *39*, 1–22. doi: 10.1016/j.preteyeres.2013.12.003

Schindelin, J., Arganda-Carreras, I., Frise, E., Kaynig, V., Longair, M., Pietzsch, T., … Cardona, A. (2012). Fiji: an open-source platform for biological-image analysis. *Nature Methods*, *9*(7), 676–682. doi: 10.1038/nmeth.2019

Shen, Y., Heimel, J. A., Kamermans, M., Peachey, N. S., Gregg, R. G., & Nawy, S. (2009). A Transient Receptor Potential-Like Channel Mediates Synaptic Transmission in Rod Bipolar Cells. *The Journal of Neuroscience*, *29*(19), 6088–6093. doi: 10.1523/jneurosci.0132-09.2009

Singer, J. H., & Diamond, J. S. (2003). Sustained Ca2+ Entry Elicits Transient Postsynaptic Currents at a Retinal Ribbon Synapse. *Journal of Neuroscience*, *23*(34), 10923–10933. doi: 10.1523/jneurosci.23-34-10923.2003

Sinha, R., Grimes, W. N., Wallin, J., Ebbinghaus, B. N., Luu, K., Cherry, T., … Hoon, M. (2021). Transient expression of a GABA receptor subunit during early development is critical for inhibitory synapse maturation and function. *Current Biology*, *31*(19), 4314-4326.e5. doi: 10.1016/j.cub.2021.07.059

Sinha, R., Siddiqui, T. J., Padmanabhan, N., Wallin, J., Zhang, C., Karimi, B., … Hoon, M. (2020). LRRTM4: A Novel Regulator of Presynaptic Inhibition and Ribbon Synapse Arrangements of Retinal Bipolar Cells. *Neuron*, *105*(6), 1007-1017.e5. doi: 10.1016/j.neuron.2019.12.028

Stockton, R. A., & Slaughter, M. M. (1989). B-wave of the electroretinogram. A reflection of ON bipolar cell activity. *The Journal of General Physiology*, *93*(1), 101–122. doi: 10.1085/jgp.93.1.101

Tachibana, M. (1999). Regulation of transmitter release from retinal bipolar cells. *Progress in Biophysics and Molecular Biology*, *72*(2), 109–133. doi: 10.1016/s0079-6107(99)00003-6

Tsuboi, A. (2020). LRR-Containing Oncofetal Trophoblast Glycoprotein 5T4 Shapes Neural Circuits in Olfactory and Visual Systems. *Frontiers in Molecular Neuroscience*, *13*, 581018. doi: 10.3389/fnmol.2020.581018

Vaegan, & Millar, T. J. (1994). Effect of kainic acid and NMDA on the pattern electroretinogram, the scotopic threshold response, the oscillatory potentials and the electroretinogram in the urethane anaesthetized cat. *Vision Research*, *34*(9), 1111–1125. doi: 10.1016/0042-6989(94)90294-1

Vardi, N., Duvoisin, R., Wu, G., & Sterling, P. (2000). Localization of mGluR6 to dendrites of ON bipolar cells in primate retina. *Journal of Comparative Neurology*, *423*(3), 402–412. doi: 10.1002/1096-9861(20000731)423:3<402::aid-cne4>3.0.co;2-e

von Gersdorff, H., & Matthews, G. (1997). Depletion and Replenishment of Vesicle Pools at a Ribbon-Type Synaptic Terminal. *Journal of Neuroscience*, *17*(6), 1919–1927. doi: 10.1523/jneurosci.17-06-01919.1997

von Gersdorff, H., Vardi, E., Matthews, G., & Sterling, P. (1996). Evidence That Vesicles on the Synaptic Ribbon of Retinal Bipolar Neurons Can Be Rapidly Released. *Neuron*, *16*(6), 1221–1227. doi: 10.1016/s0896-6273(00)80148-8

Wachtmeister, L. (1998). Oscillatory potentials in the retina: what do they reveal. *Progress in Retinal and Eye Research*, *17*(4), 485–521. doi: 10.1016/s1350-9462(98)00006-8

Wakeham, C. M., Ren, G., & Morgans, C. W. (2020). Expression and distribution of trophoblast glycoprotein in the mouse retina. *Journal of Comparative Neurology*, *528*(10), 1660–1671. doi: 10.1002/cne.24850

Wakeham, C. M., Wilmarth, P. A., Cunliffe, J. M., Klimek, J. E., Ren, G., David, L. L., & Morgans, C. W. (2019). Identification of PKCα-dependent phosphoproteins in mouse retina. *Journal of Proteomics*, *206*, 103423. doi: 10.1016/j.jprot.2019.103423

Xiong, W.-H., Pang, J.-J., Pennesi, M. E., Duvoisin, R. M., Wu, S. M., & Morgans, C. W. (2015). The Effect of PKCα on the Light Response of Rod Bipolar Cells in the Mouse Retina. *Investigative Ophthalmology & Visual Science*, *56*(8), 4961–4974. doi: 10.1167/iovs.15-16622

Xu, Y., Dhingra, A., Fina, M. E., Koike, C., Furukawa, T., & Vardi, N. (2012). mGluR6 deletion renders the TRPM1 channel in retina inactive. *Journal of Neurophysiology*, *107*(3), 948–957. doi: 10.1152/jn.00933.2011

Yoshihara, S.-I., Takahashi, H., Nishimura, N., Naritsuka, H., Shirao, T., Hirai, H., … Tsuboi, A. (2012). 5T4 Glycoprotein Regulates the Sensory Input-Dependent Development of a Specific Subtype of Newborn Interneurons in the Mouse Olfactory Bulb. *The Journal of Neuroscience*, *32*(6), 2217–2226. doi: 10.1523/jneurosci.5907-11.2012

Zanazzi, G., & Matthews, G. (2009). The Molecular Architecture of Ribbon Presynaptic Terminals. *Molecular Neurobiology*, *39*(2), 130–148. doi: 10.1007/s12035-009-8058-z

Zhao, Y., Malinauskas, T., Harlos, K., & Jones, E. Y. (2014). Structural Insights into the Inhibition of Wnt Signaling by Cancer Antigen 5T4/Wnt-Activated Inhibitory Factor 1. *Structure*, *22*(4), 612–620. doi: 10.1016/j.str.2014.01.009

Zhou, Z.-Y., Wan, Q.-F., Thakur, P., & Heidelberger, R. (2006). Capacitance Measurements in the Mouse Rod Bipolar Cell Identify a Pool of Releasable Synaptic Vesicles. *Journal of Neurophysiology*, *96*(5), 2539–2548. doi: 10.1152/jn.00688.2006